

1 **Characterization of a Thick Ozone Layer in Mars' Past**

2 J. Deighan*, R.E. Johnson

3 Engineering Physics, 395 McCormick Road, University of Virginia, Charlottesville, VA, 22904

4 USA

5 Email Addresses: jjd7v@virginia.edu*, rej@virginia.edu

6 Phone Number: 1-434-924-3244

7 **Abstract**

8 All three terrestrial planets with atmospheres support O₃ layers of some thickness. While
9 currently only that of Earth is substantial enough to be climatically significant, we hypothesize
10 that ancient Mars may also have supported a thick O₃ layer during volcanically quiescent periods
11 when the atmosphere was oxidizing. To characterize such an O₃ layer and determine the
12 significance of its feedback on the Martian climate, we apply a 1D line-by-line radiative-
13 convective model under clear-sky conditions coupled to a simple photochemical model. The
14 parameter space of atmospheric pressure, insolation, and O₂ mixing fraction are explored to find
15 conditions favorable to O₃ formation. We find that a substantial O₃ layer is most likely for
16 surface pressures of 0.3–1.0 bar, and could produce an O₃ column comparable to that of modern
17 Earth for O₂ mixing fractions approaching 1%. However, even for thinner O₃ layers, significant
18 UV shielding of the surface occurs along with feedback on both the energy budget and
19 photochemistry of the atmosphere. In particular, CO₂ condensation in the middle atmosphere is
20 inhibited and the characteristics of H₂O dissociation are modified, shifting from a direct
21 photolysis dominated state similar to modern Mars to a more Earth-like state controlled by O(¹D)
22 attack.

23

24 **Keywords:** Atmospheres, chemistry; Atmospheres, structure; Mars, atmosphere; Mars, climate;
25 Photochemistry.

26 **1. Introduction**

27 It is now known that all three atmosphere-bearing terrestrial planets—Venus, Earth, and
28 Mars—posses an O₃ layer (Montmessin et al. 2011). In the O₂ rich atmosphere of modern Earth,
29 O₃ has a significant impact on the solar and thermal radiation budgets, being the second most
30 important absorber of shortwave radiation and third most important gas affecting longwave
31 radiative forcing (Kiehl & Trenberth 1997). This results in O₃ providing substantial
32 photochemical feedback to the climate (Hauglustaine et al. 1994). Stratospheric O₃ also performs
33 the vital role of shielding surface organisms from damaging solar UV radiation. In contrast, the
34 O₃ layers observed on Venus and Mars are of scientific interest only as probes into atmospheric
35 photochemistry, being too thin to have significant climate feedback and providing hardly any UV
36 attenuation.

37 But this may not always have been the case. The terrestrial planets' atmospheres have
38 undergone major evolution since their formation (Hunten 1993), and it is known that Earth's
39 atmosphere was not always so favorable to the formation of an O₃ layer (Kasting & Donahue
40 1980). By the same token, it is possible that the other terrestrial planets may have been *more*
41 favorable to the formation of a stable O₃ layer than they are at present. If this was the case, the
42 resulting energy budget and photochemistry feedbacks could be important in understanding the
43 planets' climate evolution and habitability. In this paper we explore this possibility for Mars.

44 In order to identify conditions in Mars' past which would have favored a thick O₃ layer it
45 is important to understand the reactions governing the production and destruction of O₃.
46 Summarizing the arguments of Hiscox & Lindner (1997), we begin by examining the production
47 of O₃ via the reaction

48



49 where M is some third body, mostly likely O₂ or N₂ for Earth and CO₂ for Venus and Mars. The
50 kinetics of this reaction have a negative dependence on temperature, making O₃ production faster
51 at lower temperatures. And it is immediately obvious that increasing the concentrations [O], [O₂],
52 or [M] will increase the production rate of O₃. In the atmospheres we consider, much of the O
53 and O₂ are derived from the photolysis of CO₂, so the presence of a denser Martian atmosphere
54 will amplify the concentrations of all three species. On the other hand, destruction of the
55 oxidizing species O, O₂, and O₃ in the Martian atmosphere is largely controlled by catalytic
56 reactions involving HO_x (H, OH, HO₂) produced by H₂O photolysis. This means that a drier
57 atmosphere will have less HO_x, increasing [O] and [O₂] and reducing the destruction rate of O₃. A
58 thick and cold atmosphere will also contribute to reducing HO_x by shielding H₂O from UV and
59 lowering its vapor pressure, respectively. From this analysis, Hiscox & Lindner (1997)
60 concluded that a dense, cold, and dry atmosphere would be most favorable to the production of a
61 thick O₃ layer on Mars.

62 These conditions are somewhat at odds with those considered in many previous
63 paleoclimate studies of Mars. One of the primary drivers in studying Mars' past is explaining the
64 chemical and morphological evidence for surface modification by persistent liquid water (Carr &
65 Head 2010). Climate modeling struggles to achieve surface temperatures above 273 K simply by
66 assuming a thicker CO₂ atmosphere (Kasting 1991), and efforts to explain this discrepancy often
67 rely on additional greenhouse gases like CH₄, H₂S, and SO₂ (Halevy et al. 2009; S.S. Johnson et
68 al. 2008; Kasting 1997; Squyres & Kasting 1994). These species require a reducing atmosphere
69 and major geochemical source, conditions which are most easily met by large scale volcanic

70 activity, and result in a picture of early Mars not unlike Archean Earth (Halevy et al. 2007; S.S.
71 Johnson et al. 2009; Tian et al. 2010). Under such a warm, wet, and reducing scenario, oxidizing
72 species would be rapidly destroyed both in the atmosphere and in aqueous solution at the surface
73 (Kasting et al. 1979; Kasting & Walker 1981; Kasting et al. 1985). What little O₃ could exist
74 under such conditions would have negligible feedback on the climate.

75 However, Martian volcanism has been episodic throughout the planet's history, with the
76 most recent large scale caldera activity ending ~100–200 Ma (Neukum et al. 2010; Robbins et al.
77 2011). During volcanically quiescent geologic periods (such as the current time), any climate-
78 influencing volcanic gases would become depleted and the atmosphere would relax to a colder,
79 drier state. This would allow for the accumulation of oxidizing species such as O₂ and O₃
80 (Kasting 1995). Our characterization of O₃ climate feedback processes is pertinent to these
81 volcanically quiescent periods of Mars' history.

82 The photochemistry relevant to a thick CO₂ atmosphere lacking volcanism has been
83 examined by several authors (Hiscox & Lindner 1997; Rosenqvist & Chassefière 1995; Segura et
84 al. 2007; Selsis et al. 2002; Zahnle et al. 2008). The ability of trace amounts of a strong UV
85 absorber (SO₂) to modify the ancient Martian atmosphere's temperature structure has also been
86 demonstrated (Yung et al. 1997). However, the feedback between a photochemical product such
87 as O₃ and the planetary thermal structure has received less attention. Hiscox & Lindner (1997)
88 made the case that a Martian CO₂ atmosphere thick enough to support liquid water at the surface
89 would also produce an O₃ layer substantial enough to shield the surface from UV radiation and
90 contribute to the greenhouse effect. However, their analysis was rough and somewhat qualitative,
91 lacking detailed photochemical calculations. The studies of Rosenqvist & Chassefière (1995),

92 Segura et al. (2007), and Zahnle et al. (2008) used a fixed temperature profile for their
93 photochemical calculations. Selsis et al. (2002) did examine feedback between O₃
94 photochemistry and the temperature profile, but this was not the focus of the study and a
95 converged solution was not achieved due to excessively long run times.

96 Here we take a complementary approach, solving for the equilibrium temperature profile
97 using a radiative-convective model coupled to a simplified photochemical model. This provides a
98 first order estimate of stratospheric O₃ concentration while ensuring timely convergence. We
99 explore the parameter space of atmospheric pressure, insolation, and O₂ mixing fraction to search
100 for conditions likely to support a substantial O₃ layer and then examine the significance and
101 robustness of its feedback on the climate.

102

103 **2. Model Description**

104 2.1 Radiative-Convective Model

105 Radiative-convective equilibrium is solved for using a 1D line-by-line (LBL) model. The
106 decision to use LBL is motivated by recent concerns that standard 1D models of ancient Mars,
107 such as used by Pollack et al. (1987) and Kasting (1991), suffer from serious parameterization
108 issues (Halevy et al. 2009; L. Kaltenegger, pers. comm., 2009; Wordsworth 2010a). There has
109 also been recent work demonstrating that correlated-k parameterizations commonly used for
110 Earth result in radiative forcing by H₂O and O₃ which can deviate significantly from those given
111 by LBL calculations (Forster et al. 2011; Tvorogov et al. 2005). While LBL calculation is more
112 fundamentally correct than other methods and is important for benchmarking the accuracy of
113 alternative techniques, it has been rejected for many applications in the past because it is

114 computationally slow (Liou 2002). However, given new optimization techniques and the steady
115 advance in computing power, such models are becoming more common in planetary science
116 (Corrêa et al. 2005; Letchworth & Benner 2007; Kuntz & Höpfner 1999; Quine & Drummond
117 2002; Wells 1999).

118 In our model the atmosphere is divided into layers at a vertical resolution of 2 km, with
119 the domain extending from the planet's surface up to the altitude where atmospheric pressure
120 approaches 10^{-6} bar (0.1 Pa). The low pressure limit is chosen to avoid the complex effects
121 encountered in the upper atmosphere. These include the onset of the ionosphere, violation of
122 local thermodynamic equilibrium, transition of the dominant mass transfer mechanism from eddy
123 diffusion to molecular diffusion at the homopause, and transition of the dominant heat transfer
124 mechanism from radiation to conduction at the mesopause (Bougher et al. 2008, López-Valverde
125 et al. 1998).

126 Radiation is divided into two spectral regions: a UV region from 119 nm to 400 nm at 1
127 nm resolution and a visible/infrared (VIR) region ranging from 25000 cm^{-1} (400 nm) to 0 cm^{-1}
128 with a non-uniform grid. The resolution of the pre-computed VIR grid varies from $2^{-15}-1\text{ cm}^{-1}$ in
129 order to resolve individual radiative lines at one half-width or better, and is optimized for the
130 input parameters of a given run (i.e. surface pressure, species' concentrations). The solar
131 radiation source in the UV is taken from the ASTM E-490 reference spectrum and VIR radiation
132 uses the synthetic spectrum provided by the AER group (Clough et al. 2005), which is generated
133 from the Kurucz (1992) solar source function. Solar fluxes are scaled by 1/4th to account for
134 global and diurnal averaging. Absorption by CO_2 , H_2O , and O_3 is considered in both spectral
135 regions and O_2 is included in the UV.

136 UV cross-sections are obtained from various authors via the MPI-Mainz-UV-VIS
137 Spectral Atlas of Gaseous Molecules and Sander et al. (2011). Temperature dependent CO₂ UV
138 cross-sections are used via linear interpolation of data at 295 K and 195 K, being held constant
139 below 195 K. The temperature sensitive Schumann-Runge bands of O₂ in the UV are computed
140 via the method of Minschwaner et al. (1992) and binned at 1 nm.

141 VIR cross-sections are calculated line-by-line using the 2008 HITRAN database
142 (Rothmann et al. 2009). Pressure broadening and line shifting of H₂O lines by CO₂ instead of air
143 is implemented using the results of Brown et al. (2007). This increases pressure-broadened half-
144 widths by a factor of 1.7 on average relative to terrestrial air. Based on this, pressure-broadened
145 half-widths of O₃ lines in air are multiplied by 1.7, as data on CO₂ pressure-broadening of O₃ is
146 lacking. A Voigt line shape profile is used out to 40 Doppler half-widths from the line center and
147 beyond that a van Vleck–Weisskopf profile is used. For H₂O and O₃ a Lorentzian wing cut-off of
148 25 cm⁻¹ from the line center is used, while sub-Lorentzian CO₂ wings are treated by using
149 empirical χ -factors with a cut-off of 500 cm⁻¹ (Halevy et al. 2009; Wordsworth et al. 2010a). The
150 χ -factor of Perrin & Hartmann (1989) is used in the range 0–3000 cm⁻¹, that of Tonkov et al.
151 (1996) is used for 3000–6000 cm⁻¹, and that of Meadows & Crisp (1996) is used > 6000 cm⁻¹.

152 For H₂O and O₃ only the most common isotopologues are used (H¹⁶OH, ¹⁶O¹⁶O¹⁶O), while
153 for CO₂ the three most common isotopologues are considered (¹⁶O¹²C¹⁶O, ¹⁶O¹³C¹⁶O, ¹⁶O¹²C¹⁸O).
154 Also, for each layer weak radiative lines are excluded from calculations based on the criterion of
155 optical depth $\tau < 0.01$ at the line peak when integrated across the overhead atmospheric column.
156 These measures are taken for computational economy, and including rarer species and weaker
157 lines has a negligible (< 1 K) effect on the temperature profile.

158 Collision induced absorption (CIA) by CO₂ is accounted for using the “GBB”
159 parameterization of Wordsworth et al. (2010a), which is based on the experimental work of
160 Baranov et al. (2004) and Gruszka & Borysow (1998). The Chappuis and Wulf continua of O₃ in
161 the VIR are sampled at 1 cm⁻¹ from the MT_CKD continuum model (Clough et al. 2005).
162 Rayleigh scattering cross-sections for CO₂ are calculated from its refractive index. In the UV the
163 refractive index is taken from Bideau-Mehu et al. (1973), while in the VIR the results of Old et
164 al. (1971) are used. In both regions the King correction factor is taken from Alms et al. (1975).

165 For radiative transfer the plane-parallel approximation is used and treatment follows a
166 two-stream method, applying the technique of Toon et al. (1989) for scattering of solar radiation.
167 The planet's surface is taken to be a Lambertian reflector with an albedo of 0.20 for solar
168 radiation and an emissivity of 1.0 for thermal radiation. A moist pseudoadiabatic lapse rate is
169 used in the troposphere, with the surface as an H₂O source at a specified relative humidity (RH).
170 Above the surface the mixing fraction of H₂O is given a simple “step” profile, being held
171 constant until the condensation altitude, at which point its vapor pressure curve is followed up to
172 the cold trap based on the temperature profile. Above this the mixing fraction is again assumed to
173 be constant. Unless otherwise specified, a relatively dry surface value of RH=20% is used for all
174 the results given here, comparable to modern Mars (Zahnle et al. 2008). In regions where the
175 CO₂ atmosphere is super-saturated the lapse rate is set so that the temperature profile matches its
176 vapor pressure. Clear sky conditions are assumed.

177 For calculation of the tropospheric lapse rate, it is necessary to know the heat capacity c_p
178 of the atmosphere, dominated in this case by CO₂. From statistical mechanics, the zero-pressure
179 heat capacities of a rigidly rotating linear molecule with internal vibrational modes are

$$\frac{c_p}{R} = 1 + \frac{c_v}{R} = 1 + \frac{3}{2} + \frac{2}{2} + \sum_j \left(\frac{\theta_j}{T} \right)^2 \frac{e^{-\frac{\theta_j}{T}}}{\left(1 - e^{-\frac{\theta_j}{T}} \right)^2} \quad (1)$$

180 where R is the universal gas constant, T is the gas temperature, and θ_j is the characteristic
 181 temperature of the j th vibrational mode. For CO_2 at low planetary temperatures ($T < 373$ K) only
 182 the low energy vibrational modes $\nu_1 = 1330 \text{ cm}^{-1}$ ($\theta_1 = 1910$ K) and doubly degenerate $\nu_2 = 667$
 183 cm^{-1} ($\theta_2 = 960$ K) need to be considered. Within this temperature range, Eq. (1) produces zero-
 184 pressure c_p values in excellent agreement ($< 0.1\%$ difference) with the values generated by the
 185 NIST REFPROP program v9.0 (Lemmon 2010), which uses an elaborate CO_2 equation of state
 186 (EOS) from Span & Wagner (1996) (see Fig. 1). For $T > 140$ K it also compares well with the c_p
 187 parameterization derived from the Venusian atmosphere by Lebonnois et al. (2010). There is a
 188 greater discrepancy with the expression used by Kasting (1991), however a review of the
 189 literature reveals that this formulation originated in a paper by Eastman (1929) and is intended
 190 for application from 300–2500 K.

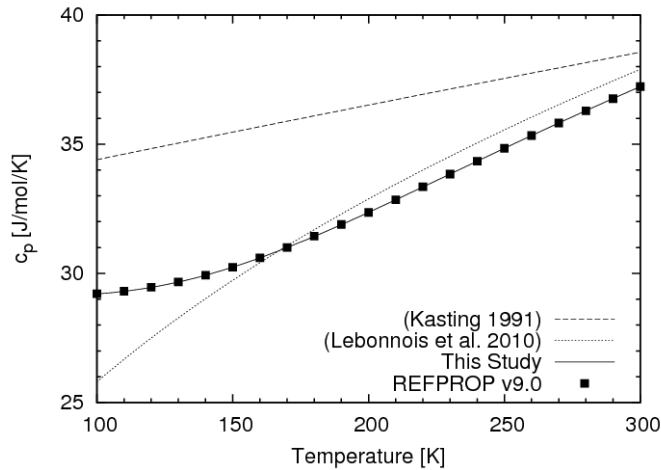


Figure 1: Comparison of CO_2 specific heat capacity formulations.

191

192 For non-zero pressures the heat capacity must be corrected for the non-ideal nature of the
 193 gas. In this we follow the appendix of Wordsworth et al. (2010b). To summarize, the Redlich-
 194 Kwong EOS of Li et al. (2006) is used, having the form

$$p = \frac{RT}{v-b} - \frac{a}{v(v-b)\sqrt{T}} \quad (2)$$

195
 196 where p is pressure, v is volume, and a and b are parameters specific to the gas under
 197 consideration. For the relatively low pressures considered here, this may be expressed as a Virial
 198 expansion

$$\frac{pv}{RT} \approx 1 + \frac{B}{v} = 1 + \frac{1}{v} \left(b - \frac{a}{RT^{3/2}} \right) \quad (3)$$

199
 200 which can be used to calculate the pressure correction to the heat capacity via the definition

$$\begin{aligned} c_p(p, T) &= c_p(0, T) - T \int_0^p \left(\frac{\partial^2 v}{\partial T^2} \right)_{p'} dp' \\ &= c_p(0, T) - T p \left(\frac{\partial^2 B}{\partial T^2} \right) \end{aligned} \quad (4)$$

201
 202 In the formulation of Li et al. (2006), the parameter a is dependent on both p and T ,
 203 having the form $a = a_1(T) + a_2(T)p$. Because of the relatively low pressures relevant to Mars' past
 204 (≤ 5 bar) we neglect the small pressure correction to a and differentiate B analytically.
 205 Calculating c_p by this method agrees well with the NIST REFPROP program over the range of
 206 pressures and temperatures considered in this study.

207 Sensitivity testing with respect to the value of c_p found that the surface temperature is not
 208 strongly affected by the use of our formulation as compared to that of Kasting (1991). Although

209 the lapse rate increases significantly, a concurrent lowering in the height of the tropopause limits
 210 the surface temperature increase to at most a few K.

211 In our model the temperature profile is solved for by iteratively calculating the net flux
 212 F_{net} for each layer in the atmosphere and then setting the net flux to zero. This is done by
 213 assuming that the absorbed flux is constant, and adjusting the emitted flux F_{emt} by changing the
 214 layer temperature T . To find the necessary step size ΔT , an estimate of the derivative dF_{emt}/dT is
 215 required. We begin by taking the emitted flux to be

$$F_{emt} = \pi \int_0^{\infty} B(\nu, T)(1 - e^{-\tau(\nu, T)}) d\nu \quad (5)$$

216
 217 By assuming that $e^{-\tau}$ has a weak dependence on temperature over the interval ΔT , we may
 218 approximate the derivative as

$$\frac{dF_{emt}}{dT} \approx \pi \int_0^{\infty} \left[\frac{dB}{dT} \right]_{\nu} (1 - e^{-\tau(\nu, T)}) d\nu \quad (6)$$

219
 220 For the conditions considered here, the radiatively active $\nu_2 = 667 \text{ cm}^{-1}$ vibrational mode of CO_2
 221 dominates thermal transfer where the atmosphere is in radiative equilibrium. This allows for two
 222 more useful approximations. First, thermal emission occurs in the high energy tail of the Planck
 223 function at the temperatures of interest ($T \ll \theta_2 = 960 \text{ K}$), allowing the simplification

$$\frac{dF_{emt}}{dT} \approx \pi \int_0^{\infty} \frac{h\nu}{kT^2} B(\nu, T)(1 - e^{-\tau(\nu, T)}) d\nu \quad (7)$$

224
 225 Second, by approximating the ν_2 emission band as a δ -function we may write

$$\frac{dF_{emt}}{dT} \approx \frac{h\nu_2}{kT^2} \pi \int_0^{\infty} B(\nu, T)(1 - e^{-\tau(\nu, T)}) d\nu \quad (8)$$

226

227 which is readily recognized as

$$\frac{dF_{emt}}{dT} \approx \frac{h\nu_2}{kT^2} F_{emt} \quad (9)$$

228

229 This simple formulation is surprisingly accurate under the conditions for which it is derived, with
230 typical errors $< 1\%$ compared to a numerical integration without approximations. After
231 application of the derived ΔT , a convective adjustment is applied in any layers where the lapse
232 rate exceeds the pseudoadiabatic lapse rate.

233 An issue with convergence by this method arises when lower layers in the atmosphere
234 become optically thick across the entire thermal IR. If there is a surplus of outgoing radiation at
235 the top of the model, adjusting the surface temperature to achieve flux balance is no longer
236 effective because changes must diffuse through the atmosphere up to space over several
237 iterations. In the meantime, the surface receives little feedback and makes further changes,
238 resulting in stability issues. This situation is typical of thick, warm, wet Martian atmospheres.
239 Since modeling these climatic conditions is of general interest, the issue must be resolved. Our
240 solution is to reduce temperatures throughout the optically thick region of the atmosphere along
241 with the surface temperature. First we find the region between the surface and the altitude where
242 the temperature drops below the planet's effective temperature T_{eff} . After the normal iteration
243 technique to balance radiative flux and convection is applied, the layer in this region with the
244 smallest ΔT value, ΔT_{min} , is identified. The temperatures of all layers in the region are then
245 adjusted

$$T_{adj} = T_{norm} - \Delta T_{min} + \Delta T_{surf} \quad (10)$$

246

247 where T_{adj} is the adjusted temperature, T_{norm} is the normal unadjusted temperature, and ΔT_{surf} is the
248 negative temperature change normally made at the surface. This technique ensures that the planet
249 cools when there is a surplus of outgoing flux, but retains the relative temperature changes
250 between atmospheric layers in each iteration.

251

252 2.2 Photochemical Model

253 The photochemical model is constructed as a series of atmospheric layers co-located with
254 those of the radiative-convective model. The concentration profiles of CO₂, CO, O₂, and H₂O are
255 fixed, while O₃, O, and O(¹D) are solved for by assuming local equilibrium. The reactions
256 considered and their rate coefficients are listed in Table 1. Photolysis rates are derived from the
257 UV/VIS flux profiles generated by the radiative-convective model, with quantum efficiencies
258 taken from the review of Sander et al. (2011). The Kinetic-PreProcessor (KPP) code is used to
259 solve for photochemical equilibrium (Daescu et al. 2003; Damien et al. 2002; Sandu et al. 2003).

260 For simplicity and clarity, eddy diffusion transport and H₂O photochemistry after
261 dissociation are neglected in the current model. While such a decision is not strictly accurate, it
262 allows feedback mechanisms not associated with these processes to be examined independently
263 and without obfuscation. The effects of neglecting these processes are most important in the
264 troposphere and have qualitatively predictable consequences. These will be addressed later in the
265 discussion.

266 For a real CO₂ atmosphere with no or little H₂O photochemistry, i.e. a “dry” atmosphere,
267 CO and O₂ produced by photodissociation would exist at a stoichiometric ratio of 2:1 and could

268 accumulate to mixing fractions of $\sim 10^{-2}$ due to the inefficiency of CO_2 recombination via k_{10} in
 269 the absence of HO_x species (McElroy & Donahue 1972; Nair et al. 1994; Parkinson & Huntent
 270 1972). Under a “humid” atmosphere (modern Mars falls into this category) the $\text{CO}:\text{O}_2$ ratio
 271 declines and the mixing fractions can be reduced by orders of magnitude (on modern Mars the
 272 ratio is roughly 1:2 with mixing fractions on the order of 10^{-3}). In addition, the planetary surface
 273 may act as a reductant source via volcanism (Kasting et al. 1979) and oxidant sink via
 274 weathering (Kasting & Walker 1981; Kasting et al. 1985; Zahnle et al. 2008). These act to
 275 increase CO concentration and decrease O_2 concentration. However, quantitatively evaluating the
 276 impact requires detailed analysis and is fraught with uncertainties about the climate,
 277 geochemistry, and volcanism of ancient Mars (Tian et al. 2010).

Reactants	Products	Rate Coefficient	Reference
$\text{CO}_2 + h\nu$	$\rightarrow \text{CO} + \text{O}$	J_1	(Sander et al. 2011)
$\text{CO}_2 + h\nu$	$\rightarrow \text{CO} + \text{O}(^1\text{D})$	J_2	(Sander et al. 2011)
$\text{O}_2 + h\nu$	$\rightarrow \text{O} + \text{O}$	J_3	(Sander et al. 2011)
$\text{O}_2 + h\nu$	$\rightarrow \text{O} + \text{O}(^1\text{D})$	J_4	(Sander et al. 2011)
$\text{O}_3 + h\nu$	$\rightarrow \text{O}_2 + \text{O}$	J_5	(Sander et al. 2011)
$\text{O}_3 + h\nu$	$\rightarrow \text{O}_2 + \text{O}(^1\text{D})$	J_6	(Sander et al. 2011)
$\text{H}_2\text{O} + h\nu$	$\rightarrow \text{H} + \text{OH}$	J_7	(Sander et al. 2011)
$\text{O}(^1\text{D}) + \text{CO}_2$	$\rightarrow \text{CO}_2 + \text{O}$	$k_8 = 1.63 \times 10^{-10} e^{60/T}$	(Sander et al. 2011)
$\text{O}(^1\text{D}) + \text{H}_2\text{O}$	$\rightarrow \text{HO} + \text{HO}$	$k_9 = 7.5 \times 10^{-11} e^{115/T}$	(Sander et al. 2011)
$\text{CO} + \text{O} + \text{M}$	$\rightarrow \text{CO}_2 + \text{M}$	$k_{10} = 2.2 \times 10^{-33} e^{-1780/T}$	(Inn 1974)
$\text{O} + \text{O} + \text{M}$	$\rightarrow \text{O}_2 + \text{M}$	$k_{11} = 2.5 \times 4.8 \times 10^{-33} (300/T)^{2*}$	(Campbell & Gray 1973)
$\text{O} + \text{O}_2 + \text{M}$	$\rightarrow \text{O}_3 + \text{M}$	$k_{12} = 2.5 \times 6.0 \times 10^{-34} (300/T)^{2.4*}$	(Sander et al. 2011)
$\text{O} + \text{O}_3$	$\rightarrow \text{O}_2 + \text{O}_2$	$k_{13} = 8.0 \times 10^{-12} e^{-2060/T}$	(Sander et al. 2011)

Table 1: Photochemical Reactions

278 * Rate constant multiplied by 2.5 for increased efficiency of CO_2 as third body.

279

280 For the purposes of this paper we simply assume that the CO:O₂ ratio is of order unity
281 and a range of prescribed mixing fractions from 10⁻⁵ to 10⁻² is examined for these species. Based
282 on the work of Kasting & Donahue (1980), which quantified the impact of an O₃ layer on ancient
283 Earth, within this range O₂ should be stable enough against catalytic destruction by HO_x to
284 maintain a roughly constant mixing fraction at all altitudes. This range of mixing fractions is also
285 consistent with the CO₂-H₂O photochemical modeling results of Rosenqvist & Chassefière
286 (1995), and thus is appropriate for a low volcanic outgassing rate and slow surface weathering
287 under a cold, dry climate (Kasting 1995).

288

289 **3. Results & Discussion**

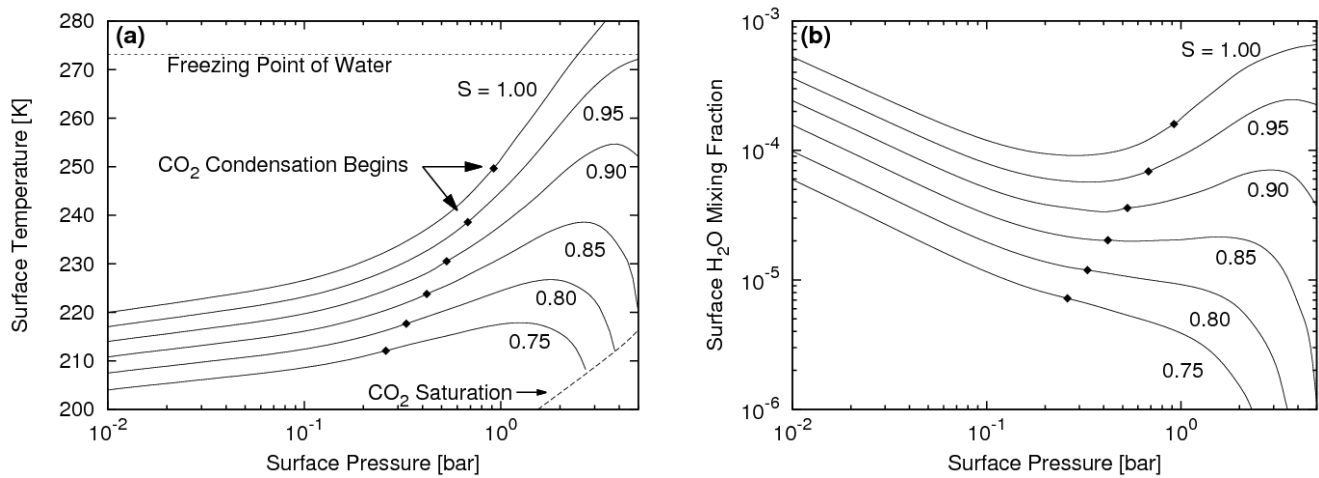
290 3.1 Comparison with Previous Radiative-Convective Models

291 As a validation of the radiative-convective model some test runs were performed without
292 photochemistry to compare with the results of selected models in the literature. Under modern
293 insolation a surface temperature of 273 K is achieved for a surface pressure of 2.5 bar, somewhat
294 higher than the 2.2 bar reported by Pollack et al. (1987). This may be explained by our inclusion
295 of CO₂ condensation (Kasting 1991) and differing treatment of CIA parameterization
296 (Wordsworth et al. 2010a). The differences in H₂O profile structure and surface albedo between
297 the two models also have minor influences. To compare with the model of Wordsworth et al.
298 (2010a), the insolation is scaled by a factor of 0.75 at all wavelengths to approximate early solar
299 conditions and H₂O is removed from the atmosphere. Under these conditions a peak surface
300 temperature of 215 K is found at a surface pressure of ~ 1 bar, and condensation of the

301 atmosphere at the surface occurs near a temperature of 208 K and pressure of just over 2.7 bar.
 302 These results are comparable to those of Wordsworth et al. (2010a) for their “GBB” CIA
 303 parameterization (Baranov et al. 2004; Gruszka & Borysow 1998) with sub-Lorentzian wings for
 304 CO₂ lines. This is encouraging, as this model is the most similar to ours in the calculation of
 305 radiative cross-sections.

306

307 3.2 Parameter Space Study Without Photochemistry



308 **Figure 2: Parameter space showing (a) surface temperature and (b) surface H₂O mixing**
 309 **fraction as a function of surface pressure P and insolation S (for modern Sun intensity $S =$**
 310 **1.00). For each S track the pressure above which CO₂ condensation begins in the middle**
 311 **atmosphere is indicated by ◆.**

312

313 To guide our search for atmospheres that would have been most conducive to the
 314 formation of O₃, we first use the radiative-convective model with no photochemistry to explore
 315 the parameter space of surface pressure P and insolation S , where S is the insolation as a fraction

316 of modern intensity. A plot of the resulting surface temperature is shown in Fig. 2a, with the
317 diamond symbols identifying for each value of S at what surface pressure CO_2 condensation
318 begins in the middle atmosphere. Unlike the model of Kasting (1991), which produced CO_2
319 condensation at modern insolation levels for $P \geq 0.35$ bar, our model (without photochemistry)
320 does not condense until $P \geq 0.92$ bar. This discrepancy is likely due to the differing treatment of
321 NIR solar absorption between the models, with ours having greater stratospheric heating (J. F.
322 Kasting & R. Ramirez, pers. comm., 2011). It is worth noting that both models calculate a
323 globally averaged temperature profile and assume radiative-convective equilibrium. CO_2
324 condensation could still occur for $P < 0.92$ bar, as it does on Mars today, in cold regions at high
325 latitude (Kelly et al. 2006) and in the mesosphere due to temperature fluctuations driven by
326 atmospheric waves (Montmessin et al. 2006).

327 Surface H_2O mixing fraction $f_{\text{H}_2\text{O}}$ is shown in Fig. 2b as a function of P and S . It may be
328 seen that for $S > 0.85$ there exists a local minimum for $f_{\text{H}_2\text{O}}$. The reason for this minimum is as
329 follows: For $P < 0.3$ bar the surface temperature increases only weakly with pressure, causing the
330 vapor pressure of H_2O to rise less quickly than the CO_2 pressure and resulting in the decline of
331 $f_{\text{H}_2\text{O}}$. At $P > 0.3$ bar H_2O becomes an important greenhouse gas for these atmospheres and its
332 positive feedback on temperature is strong enough to increase $f_{\text{H}_2\text{O}}$ with increasing surface
333 pressure. For $S < 0.85$ the surface temperature never rises enough for H_2O to become a
334 significant greenhouse gas, and so its mixing fraction decreases monotonically with P .

335 For the purpose of identifying conditions likely to support a thick O_3 layer, it is of interest
336 to summarize here some of the results of Rosenqvist & Chassefière (1995). Modeling a CO_2 - H_2O
337 atmosphere with a fixed temperature profile and varying pressure, they identified three distinct

338 photochemical regimes for the O₂ mixing fraction f_{O_2} , which may be compared with those for f_{H_2O}
339 outlined above. For $P < 0.1$ bar f_{O_2} declined with P , while for $0.1 < P < 1$ bar it rose with P , and
340 finally declined again at $P > 1$ bar. The cause of rising f_{O_2} for $0.1 \text{ bar} < P < 1 \text{ bar}$ was determined
341 to be increased shielding of H₂O against photolysis, resulting in decreased destruction of O₂ by
342 HO_x. By $P \sim 1$ bar this caused the atmospheric photochemistry to be insensitive to H₂O content.
343 For $P < 1$ bar they found that artificially reducing f_{H_2O} (making the atmosphere drier) also
344 reduced HO_x and produced a higher f_{O_2} .

345 Taking the results presented above concerning pressure and temperature with no
346 photochemistry along with those of Rosenqvist & Chassefière (1995) concerning pressure at
347 fixed temperature, it would seem that conditions favorable to O₃ formation are most likely to be
348 found at moderate pressures of 0.3–1.0 bar. The lower end of this range corresponds with our
349 finding of a minimum mixing fraction of tropospheric H₂O for pressures ≥ 0.3 bar, while the
350 upper end is determined by the finding of Rosenqvist & Chassefière (1995) that tropospheric
351 H₂O is increasingly shielded as pressures approach 1 bar. Thus, within this range we expect a
352 minimum of H₂O photolysis, with a corresponding maximum in accumulation of oxidizing
353 species like O₂ and O₃.

354 In a broader context, focusing on atmospheric pressures of 0.3–1.0 bar is consistent with
355 recent work suggesting that Mars had an atmosphere ≥ 0.2 bar at some time in its past (Manga et
356 al. 2012) but has volcanically outgassed ≤ 1 bar CO₂ over its history (Grott et al. 2011). It is also
357 notable that this range falls within the 0.1–1 bar “dead zone” in Mars' history identified by
358 Richardson & Mischna (2005). That study pointed out that within this range of pressures diurnal
359 temperature highs would rarely reach the freezing point of water. Subsequently, loss of CO₂ by

360 surface weathering would be limited, reducing its utility for explaining the modern observed
361 pressure of 6 mbar. For climates in this “dead zone” we expect that feedback from O₃ would be
362 relatively strong. If a significant positive effect on surface temperature exists, warming by O₃
363 might have helped stabilize ephemeral liquid water, facilitating continued weathering out of CO₂.
364 We consider this possibility when investigating the effect of O₃ on the energy budget.

365

366 3.3 Parameter Space Study With Photochemistry

367 Based on the results of the previous section, and in order to more directly compare with
368 previous work by Selsis et al. (2002), we select our nominal atmospheric model to have an O₂
369 mixing fraction $f_{O_2} = 10^{-3}$ with surface pressure $P = 1$ bar and a modern insolation intensity $S =$
370 1.00. We then vary f_{O_2} , P , and S in turn to characterize their effect on the O₃ layer and its
371 feedbacks.

372

373 3.3.1 O₃ Profile and Column

374 We begin our characterization of potential Martian O₃ layers by examining their
375 concentration profiles and integrated column densities. Varying f_{O_2} , we find that with more O₂ the
376 O₃ layer becomes thicker and its peak value larger and located at higher altitude (Fig. 3). This
377 same behavior has been found by models examining the photochemistry of early Earth (Kasting
378 & Donahue 1980), and is due to the increased availability of O₂ for O₃ production and decreased
379 penetration of UV. In contrast, we find that varying P and S have little effect on the profile when
380 altitude is plotted as pressure (not shown).

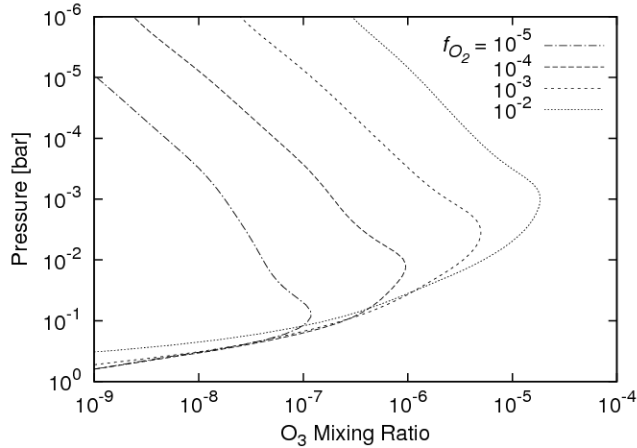


Figure 3: O₃ profiles for various f_{O_2} in a 1 bar atmosphere under modern insolation.

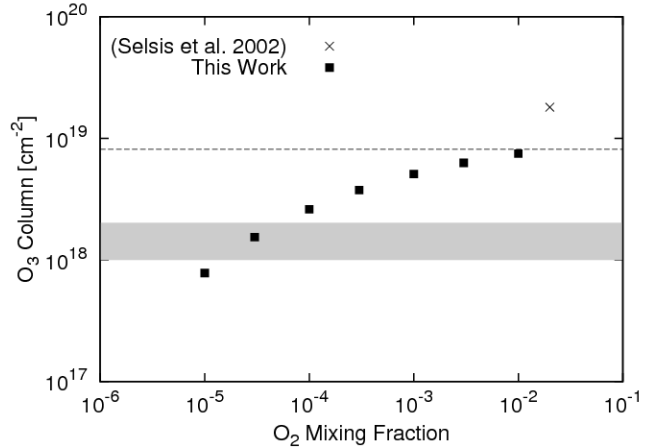


Figure 4: O₃ column as a function of f_{O_2} . The dashed line is a typical column on modern Earth ($8.1 \times 10^{18} \text{ cm}^{-2}$), and the shaded region estimates the column necessary to protect bacteria from UV radiation (François & Gérard 1988).

382 While increasing f_{O_2} generally increases the O₃ column (Fig. 4), it eventually levels off at
 383 a value comparable to that of modern Earth ($300 \text{ Dobson units} \approx 8.1 \times 10^{18} \text{ cm}^{-2}$). Again, this is in
 384 line with models of the early Earth (Kasting & Donahue 1980). We obtain an O₃ column of
 385 $7.5 \times 10^{18} \text{ cm}^{-2}$ for our most oxidizing atmosphere with $f_{O_2} = 1 \times 10^{-2}$. This is less than half of the
 386 $1.8 \times 10^{19} \text{ cm}^{-2}$ column of the “*super ozone layer*” reported by Selsis et al. (2002) for a 1 bar
 387 Martian atmosphere with $f_{O_2} = 2 \times 10^{-2}$. While our results are not directly comparable with those
 388 of Selsis et al. (2002) due to the different f_{O_2} , as previously mentioned we expect our O₃ column
 389 to be little different for higher f_{O_2} . Curiously, since the model of Selsis et al. (2002) contains
 390 catalytic HO_x destruction of O₃ and ours does not, we would expect their model to produce a
 391 column smaller than ours, not larger. Furthermore, both models contain the majority of their O₃

392 in the stratosphere, so the detailed tropospheric photochemistry implemented in Selsis et al.
393 (2002) cannot be the cause of disagreement. We considered the possibility that the difference was
394 due to our diurnal averaging of solar flux for photochemistry (Krasnopolsky 2006), but a test run
395 using average daytime insolation increases our O₃ column by only 10%. The model's
396 insensitivity to solar flux also rules out the disagreement being caused simply by a differing
397 choice in solar zenith angle (Kasting & Donahue 1980). We conclude that the discrepancy most
398 likely comes about because the result of Selsis et al. (2002) is not a converged solution, and
399 should only be considered as an upper limit. Our simple converged model thus provides a tighter
400 constraint on the maximum stratospheric O₃ column in a thick Martian atmosphere, limiting it to
401 very nearly the same value as on Earth.

402 In the interest of assessing the potential habitability of these Martian atmospheres for
403 primitive life, an estimate for the minimum O₃ column necessary to ensure bacterial survival
404 from UV damage is included in Fig. 4. We follow Hiscox & Lindner (1997) in taking the
405 minimum tolerable O₃ column range determined for Earth by François & Gérard (1988) and
406 scaling it to account for the lower UV flux at Martian orbit. We find that, under this globally
407 averaged, clear sky, 1 bar CO₂ atmosphere with modern insolation, surface UV conditions
408 capable of allowing bacterial survival require $f_{O_2} > 10^{-5}$. Including clouds and dust in the
409 atmosphere would further reduce the UV flux at the surface. It should also be noted that in the
410 early solar system, the UV flux from the young Sun was generally less than that of the modern
411 Sun at $\lambda > 200$ nm and greater at $\lambda < 200$ nm (Ribas et al. 2010). Since CO₂ absorbs virtually all
412 radiation at $\lambda < 200$ nm regardless of O₂ and O₃ column, the use of a modern solar spectrum by
413 François & Gérard (1988) somewhat overestimates the minimum O₃ column required to support

414 primitive surface life on Mars under the young Sun.

415

416 3.3.2 Energy Budget

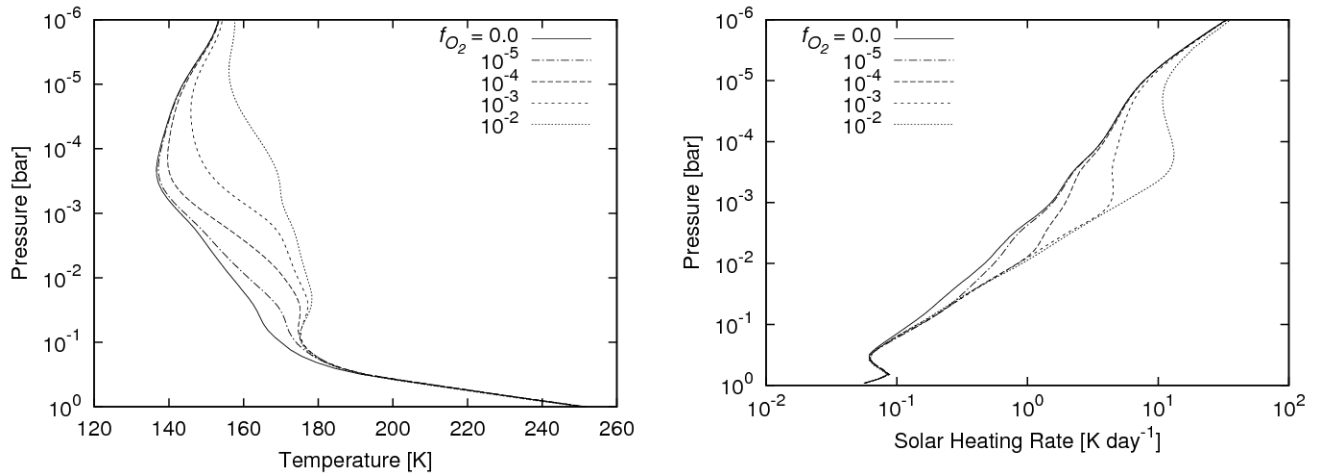


Figure 5: Temperature profile for various f_{O_2} in a 1 bar atmosphere under modern insolation. Figure 6: Solar heating profile for various f_{O_2} in a 1 bar atmosphere under modern insolation.

417 While temperatures in the middle atmosphere strongly increase with more O₂ due to
418 increased solar absorption by the O₃ layer, the surface temperature is not greatly affected (Fig. 5).
419 Testing with the removal of the O₃ IR bands resulted in a surface temperature drop of at most ~ 1
420 K, indicating that the contribution of O₃ to the greenhouse effect in these models is weak. Solar
421 absorption by thin O₃ layers primarily cause heating just above the tropopause, and the altitude
422 and magnitude of peak solar heating by O₃ rises with increasing O₂ (Fig. 6). The majority of this
423 heating is due to absorption in the UV/VIS wavelengths, as on Earth, and occurs above the 0.1
424 bar pressure level in the atmosphere where Rayleigh scattering becomes important. As a result,
425 the planetary bond albedo is significantly reduced, with a decrease of 8.1% at $f_{O_2} = 10^{-2}$ relative
426 to an atmosphere without an O₃ layer. This corresponds to a 3.8% increase in solar energy

427 absorbed by the planet. The portion of this energy injected into the upper troposphere suppresses
 428 the thermal convective flux, resulting in a small warming effect at the surface. However, for
 429 thick O₃ layers this is counteracted by an overall reduction in the amount of solar radiation
 430 reaching the surface, as the majority of the O₃ absorption occurs high in the atmosphere and is
 431 simply re-radiated to space thermally. A listing of convective, longwave, and shortwave fluxes at
 432 the surface and top of the atmosphere for various values of f_{O_2} are given in Table 2.

433

f_{O_2}	$\Delta F_{\uparrow, surf}^C$	$\Delta F_{\downarrow, surf}^L$	$\Delta F_{\downarrow, surf}^S$	$\Delta F_{\uparrow, top}^S$
10^{-5}	-0.3 (-0.6%)	+2.2 (+1.1%)	-0.6 (-0.6%)	-1.4 (-2.9%)
10^{-4}	-0.6 (-1.2%)	+2.7 (+1.4%)	-1.3 (-1.3%)	-2.4 (-5.1%)
10^{-3}	-1.6 (-3.2%)	-0.4 (-0.2%)	-1.9 (-2.0%)	-3.2 (-6.8%)
10^{-2}	-2.3 (-4.8%)	-3.7 (-1.9%)	-2.4 (-2.5%)	-3.8 (-8.1%)

Table 2: Effect of varying f_{O_2} on O₃ energy budget forcing for $P = 1$ bar, $S = 1.00$. Each ΔF is taken with respect to the atmosphere with $f_{O_2} = 0$ and as has units of W/m². Superscripts C = convective, L = longwave, and S = shortwave.

434

435 Holding $f_{O_2} = 10^{-3}$ and lowering S below 1.00 enhances the suppression of convection and
 436 alters the change in downward surface IR flux from a slight decrease to an increase (Table 3). In
 437 contrast, approximately constant relative reductions in the amount of solar radiation reaching the
 438 surface and reflecting to space are maintained, so the net effect of reducing S is to enhance the
 439 relative surface warming effect of O₃. This suggests O₃ could act to buffer surface temperature
 440 against reductions in solar flux, although the effect is very weak for the model considered here.

441

S	$\Delta F_{\uparrow, surf}^C$	$\Delta F_{\downarrow, surf}^L$	$\Delta F_{\downarrow, surf}^S$	$\Delta F_{\uparrow, top}^S$
1.00	-1.6 (-3.2%)	-0.4 (-0.2%)	-1.9 (-2.0%)	-3.2 (-6.8%)
0.95	-1.4 (-3.3%)	+0.8 (+0.5%)	-1.9 (-2.0%)	-3.1 (-6.9%)
0.90	-1.3 (-3.5%)	+2.1 (+1.5%)	-1.9 (-2.1%)	-3.0 (-7.0%)
0.85	-1.2 (-3.8%)	+2.6 (+2.1%)	-1.9 (-2.1%)	-2.8 (-7.1%)
0.80	-1.2 (-4.8%)	+2.3 (+2.2%)	-1.7 (-2.1%)	-2.7 (-7.1%)
0.75	-1.3 (-6.2%)	+2.0 (+2.4%)	-1.6 (-2.1%)	-2.6 (-7.2%)

Table 3: Effect of varying S on O_3 energy budget forcing for $P = 1$ bar, $f_{O_2} = 10^{-3}$. Each ΔF is taken with respect to the atmosphere with $f_{O_2} = 0$ and as has units of W/m^2 . Superscripts are the same as in Table 2.

442

443 We also examine the effect of O_3 heating on CO_2 condensation in the middle atmosphere.
444 Fig. 7 shows that while a 1 bar atmosphere with $f_{O_2} = 0$ at $S = 1.00$ condenses near the 0.1 bar
445 level, an atmosphere with $f_{O_2} = 10^{-3}$ does *not* due to heating by O_3 . And though CO_2 condensation
446 is not completely suppressed at very low insolation ($S = 0.75$), it does continue to be inhibited at
447 altitudes above the 0.1 bar level. This finding likely has ramifications for the ability of CO_2
448 clouds to warm the surface through scattering of IR (Forget & Pierrehumbert 1997; Mischna et
449 al. 2000), though accurately quantifying the effect would require detailed microphysical
450 modeling (Colaprete & Toon 2003).

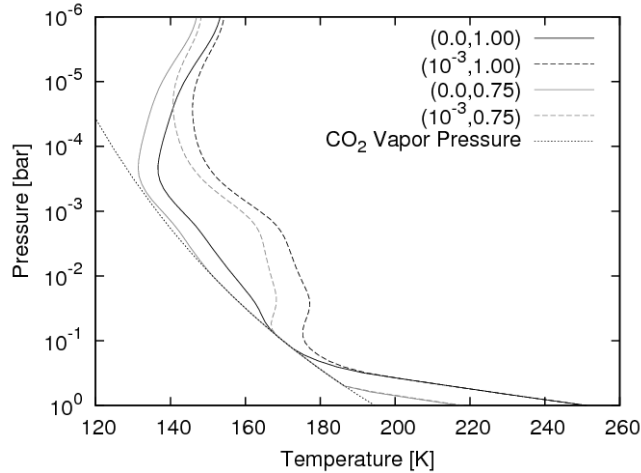
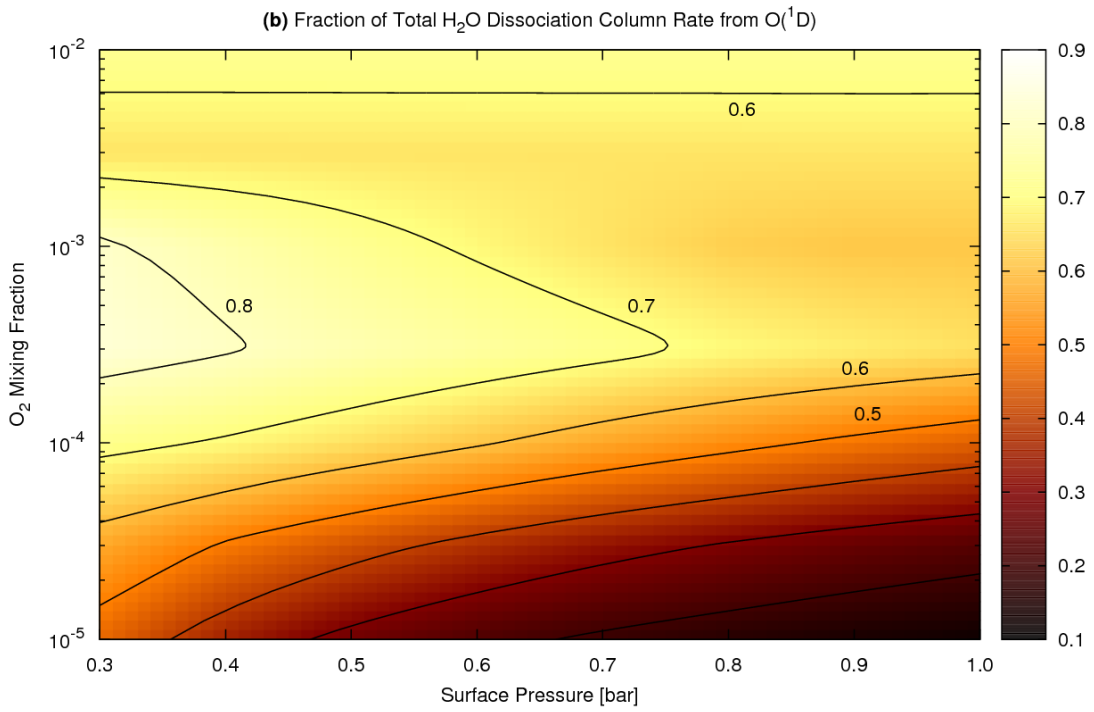
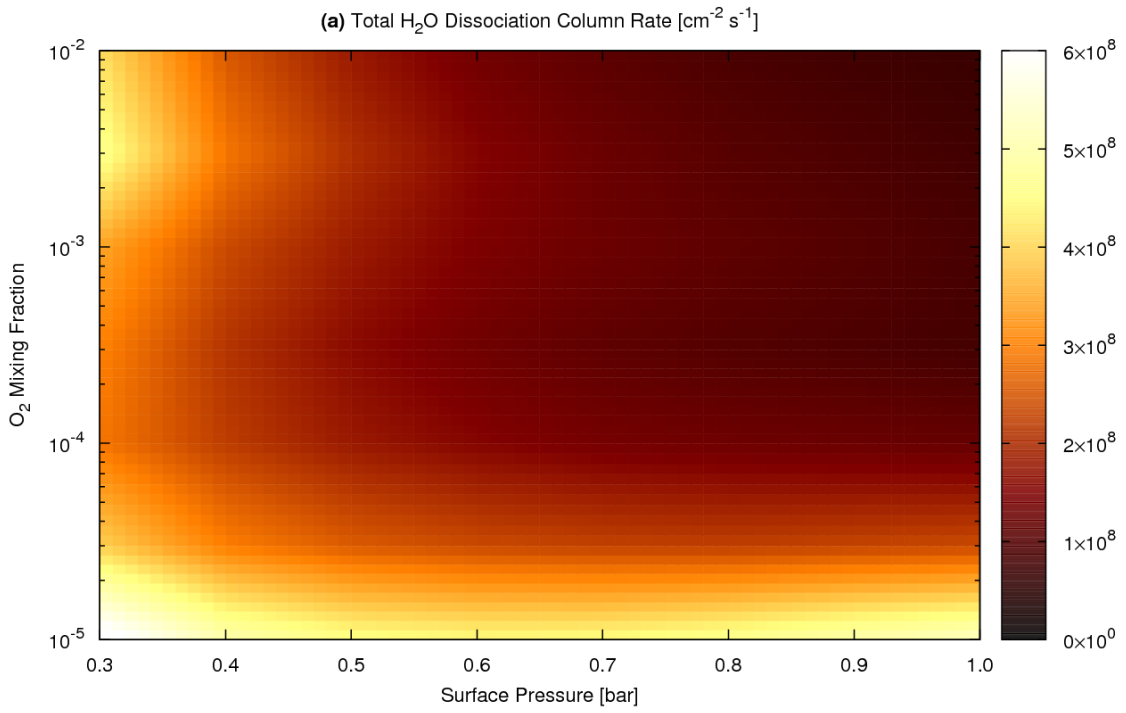


Figure 7: Temperature profiles for $f_{O_2} = 0$ and 1×10^{-3} in a 1 bar atmosphere with $S = 1.00$ and 0.75 . Line titles are in the format (f_{O_2}, S) .

451 3.3.3 H₂O Dissociation

452 The effect of O₃ on the column integrated H₂O dissociation rate is important because it
 453 plays a role in both the atmosphere's photochemistry and its loss over time. In general, the
 454 greater the amount of dissociation, the more the atmosphere will be dominated by the chemistry
 455 of HO_x products and the more H₂ will be produced. Increasing the concentration of H₂ in the
 456 atmosphere directly increases its loss rate to space and thus the loss rate of H₂O from Mars,
 457 regardless of whether loss of H₂ is limited by the escape rate of H or diffusion of H₂ at the
 458 homopause (R.E. Johnson et al. 2008; Zahnle et al. 2008). The concentration of H₂ in the upper
 459 atmosphere can also indirectly affect the loss of other species by shielding them from the EUV
 460 which powers their non-thermal escape mechanisms (Fox 2003).

461



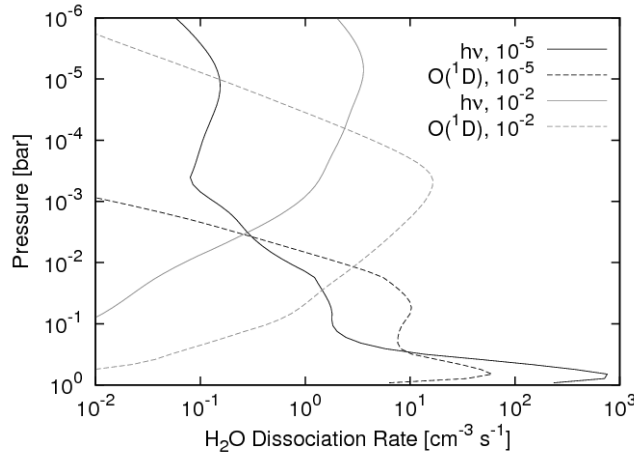
463 **Figure 8: Characterization of H₂O dissociation as a function of f_{O_2} and P : (a) total column**
464 **integrated dissociation rate (photolysis + O(¹D) attack) and (b) fraction of dissociation**
465 **attributable to O(¹D) attack.**

466

467 As seen in Table 1, the two pathways by which H₂O may be dissociated are direct
468 photolysis by UV and attack by O(¹D). The vast majority of O(¹D) in our models was produced
469 by photolysis of O₃ (J_6). In Fig. 8 we map the total column integrated H₂O dissociation rate and
470 the fraction dissociated by O(¹D) in the parameter space of P and f_{O_2} . In low pressure
471 atmospheres the column integrated O(¹D) attack rate is large because the low altitude O₃ layer
472 produces abundant O(¹D) near the H₂O rich upper troposphere. However, for high pressure
473 atmospheres the O₃ layer is raised up into the H₂O poor stratosphere, reducing the contribution of
474 O(¹D) attack to H₂O dissociation. For $f_{O_2} \sim 10^{-5}$ – 10^{-4} the O₃ layer provides little UV shielding, so
475 the direct photolysis rate of H₂O is large at all surface pressures and tends to dominate
476 dissociation. In the range $f_{O_2} \sim 10^{-4}$ – 10^{-3} a substantial O₃ layer accumulates and strongly
477 suppresses H₂O photolysis. This lowers the total dissociation rate and causes O(¹D) attack to
478 dominate at all surface pressures. When $f_{O_2} \sim 10^{-3}$ – 10^{-2} a thick O₃ layer forms. At low surface
479 pressure this strongly heats the cold trap, allowing more H₂O into the stratosphere where it can
480 be directly photolyzed or attacked by O(¹D). This enhancement in dissociation is not seen in high
481 pressure atmospheres because the O₃ layer is high above the cold trap and warms it only weakly.

482 The details of these effects are illustrated for a 1 bar atmosphere in Fig. 9. We see that for
483 low f_{O_2} most H₂O dissociation occurs by photolysis in the lower troposphere, similar to modern
484 Mars (Nair et al. 1994). On the other hand, for high f_{O_2} dissociation by O(¹D) attack becomes

485 dominant, as on modern Earth (Levy 1971). This is due to the shielding of direct H₂O photolysis
 486 by O₃ UV absorption and the enhanced production of O(¹D) by photolysis of O₃. The shielding of
 487 H₂O is partially counteracted by humidification of the stratosphere, increasing the rate of H₂O
 488 photolysis above the O₃ layer.
 489



490 **Figure 9: Comparison of H₂O dissociation profiles by photolysis and O(¹D) attack for $f_{O_2} =$**
 491 **10^{-5} and 10^{-2} . Line titles are in the format (dissociation type, f_{O_2}).**

492

493 3.3.4 Effects of HO_x and Transport

494 In the results presented here we have consciously omitted the effects of HO_x chemistry
 495 and atmospheric transport on the O₃ profile. These effects are especially important in the upper
 496 troposphere, where the radiative forcing of O₃ is most sensitive to its concentration (Forster &
 497 Shine 1997) and heating of the cold trap can influence stratospheric photochemistry. We expect
 498 our model to overestimate the stratospheric O₃ concentration due to neglecting catalytic
 499 destruction by HO_x and downward transport to the troposphere. Conversely, we underestimate

500 the tropospheric O₃ concentration because of the neglect of downward transport from the
501 stratosphere, though this would be partially counteracted by HO_x reactions. In terms of climate
502 forcing, this means that cooling by stratospheric O₃ is too large and warming by tropospheric O₃
503 too low. This suggests that the current results *underestimate* the climate warming effect of O₃
504 under the conditions examined.

505 In the results presented here, the peak O₃ concentration is always above the tropopause.
506 The location of this peak is determined by where the overhead column of O₃ absorbs most of the
507 UV capable of splitting CO₂ and O₂ to O, thus cutting off the means of O₃ production (Chapman
508 1930). Including catalytic HO_x destruction would reduce the O₃ column at a given altitude in the
509 stratosphere, in turn lowering the altitude of peak O₃ concentration. This descent of the O₃ layer
510 into the upper troposphere would strengthen some of the feedback effects identified in this study,
511 such as inhibiting CO₂ condensation and enhancing H₂O dissociation. Including convective
512 transport of O₃ from the stratosphere to the troposphere would have similar effects.

513 Taking into account the impact that O₃ can have on the H₂O dissociation rate, and vice
514 versa, it is clear that a detailed model including HO_x photochemistry and O₃ transport is needed
515 to more accurately characterize the feedback of an O₃ layer on Martian climate. Such
516 improvements will also allow us to calculate concentrations for O₂ and CO instead of using a
517 prescribed range of values, narrowing the parameter space to explore. This work is currently
518 underway.

519

520

521

522 4. Conclusions

523 We have explored here the possibility of a substantial O₃ layer accumulating in the
524 Martian atmosphere for O₂ mixing fractions of 10⁻⁵ to 10⁻², a range reasonable during the
525 volcanically quiescent periods of Mars' history. Our study focused on atmospheres with surface
526 pressures of 0.3–1.0 bar, as they are likely to have less HO_x and thus more O₂ and O₃. We find
527 that for modest O₂ mixing fractions of $f_{\text{O}_2} > 10^{-5}$ an O₃ layer capable of effectively protecting
528 primitive life from UV radiation would form. As f_{O_2} approaches 10⁻² the O₃ column becomes
529 comparable to that of modern Earth ($\sim 10^{19}$ cm⁻²).

530 The presence of a thick O₃ layer decreases planetary albedo, up to 8.1% for a 1 bar
531 atmosphere with O₃ column $\sim 10^{19}$ cm⁻². A portion of this extra heating goes toward inhibiting
532 CO₂ condensation and weakening convection, both of which act to warm the surface for the clear
533 sky conditions examined. However, for thick O₃ layers this surface warming is largely
534 counteracted by stratospheric absorption of solar energy, which efficiently radiates back into
535 space energy which otherwise would have reached the surface. Contribution of O₃ to the
536 greenhouse effect is small under the conditions examined, with a surface temperature increase of
537 only ~ 1 K. However, the net surface warming effect is likely underestimated due to our O₃
538 layers being biased toward higher altitudes. This results from the simplifications of neglecting
539 HO_x and eddy mixing in our photochemical model.

540 We also show that O₃ has a major influence on the column integrated dissociation rate of
541 H₂O by decreasing UV radiation in the lower atmosphere, increasing the production of O(¹D),
542 and increasing stratospheric humidity. Increasing the thickness of the O₃ layer causes H₂O
543 dissociation to shift from a “modern-Mars-like” state dominated by direct photolysis near the

544 surface to a “modern-Earth-like” state where photolysis is strongly suppressed and O(¹D) attack
545 becomes dominant. For atmospheres > 0.5 bar, an increase in the thickness of the O₃ layer
546 generally lowered the H₂O dissociation rate, with rates at $f_{O_2} = 1 \times 10^{-2}$ being $\sim 1/10^{\text{th}}$ their value
547 at $f_{O_2} = 1 \times 10^{-5}$. This suggests the presence of a thick O₃ layer in Mars' past could have suppressed
548 the photochemical production of H₂, and, consequently, the loss of H₂O to space. However, a
549 more complete photochemical model is required to make a definitive assessment of how a thick
550 O₃ layer would affect H₂ production on ancient Mars.

551

552 **Acknowledgments**

553 Thanks are given to D. Crisp, J. F. Kasting, and R. Ramirez for their helpful input on the
554 radiative-convective model. This work was supported by a grant from the NASA Planetary
555 Atmosphere program.

556 **References**

557

558 Alms, G.R., Burnham, A.K., Flygare, W.H., 1975. Measurement of the dispersion in
559 polarizability anisotropies. J. Chem. Phys. 63, 3321–3326. doi:[10.1063/1.431821](https://doi.org/10.1063/1.431821)

560

561 Baranov, Y.I., Lafferty, W.J., Fraser, G.T., 2004. Infrared spectrum of the continuum and dimer
562 absorption in the vicinity of the O₂ vibrational fundamental in O₂/CO₂ mixtures. J. Mol.
563 Spectr. 228, 432–440. doi:[10.1016/j.jms.2004.04.010](https://doi.org/10.1016/j.jms.2004.04.010)

564

565 Bideau-Mehu, A., Guern, Y., Abjean, R., Johannin-Gilles, A., 1973. Interferometric
566 determination of the refractive index of carbon dioxide in the ultraviolet region. Opt.
567 Commun. 9, 432–434. doi:[10.1016/0030-4018\(73\)90289-7](https://doi.org/10.1016/0030-4018(73)90289-7)

568

569 Bougher, S.W., Bledly, P.L., Combi, M., Fox, J.L., Mueller-Wodarg, I., Ridley, A., Roble, R.G.,
570 2008. Neutral Upper Atmosphere and Ionosphere Modeling. Space Science Reviews 139,
571 107–141. doi: [10.1007/s11214-008-9401-9](https://doi.org/10.1007/s11214-008-9401-9).

572

573 Brown, L.R., Humphrey, C.M., Gamache, R.R., 2007. CO₂-broadened water in the pure rotation
574 and v₂ fundamental regions. J. Mol. Spectr. 246, 1–21. doi:[10.1016/j.jms.2007.07.010](https://doi.org/10.1016/j.jms.2007.07.010)

575

576 Campbell, I.M., Gray, C.N., 1973. Rate constants for O(³P) recombination and association with
577 N(⁴S). Chem. Phys. Let. 18, 607–609. doi:[10.1016/0009-2614\(73\)80479-8](https://doi.org/10.1016/0009-2614(73)80479-8)

578

579 Carr, M., Head, J. W., 2010. Geologic history of Mars. *Earth Planet. Sci. Lett.* 294, 185-203.

580 doi:[10.1016/j.epsl.2009.06.042](https://doi.org/10.1016/j.epsl.2009.06.042)

581

582 Chapman, S., 1930. A Theory of Upper-Atmospheric Ozone. *Memoirs of the Royal*
583 *Meteorological Society* 3, 103–125.

584

585 Clough, S.A., et al., 2005. Atmospheric radiative transfer modeling: a summary of the AER
586 codes. *JQSRT* 91, 233–244. doi:[10.1016/j.jqsrt.2004.05.058](https://doi.org/10.1016/j.jqsrt.2004.05.058)

587

588 Colaprete, A., Toon, O.B., 2003. Carbon dioxide clouds in an early dense Martian atmosphere.

589 *JGR* 108, 5025. doi:[10.1029/2002JE001967](https://doi.org/10.1029/2002JE001967)

590

591 Corrêa, M.P., Souza, R.A.F., Ceballos, J.C., Fomin, B., 2005. Preliminary results of simulations
592 of a user-friendly fast line-by-line computer code for simulations of satellite signal. *Anais*
593 *XII Simpósio Brasileiro de Sensoriamento Remoto, Goiânia, Brasil, INPE*, 363–370.

594

595 Daescu, D., Sandu, A., Carmichael, G.R., 2003. Direct and Adjoint Sensitivity Analysis of
596 Chemical Kinetic Systems with KPP: II – Validation and Numerical Experiments,
597 *Atmospheric Environment* 37, 5097–5114. doi:[10.1016/j.atmosenv.2003.08.020](https://doi.org/10.1016/j.atmosenv.2003.08.020)

598

599 Damian, V., Sandu, A., Damian, M., Potra, F., Carmichael, G.R., 2002. The Kinetic PreProcessor

600 KPP – A Software Environment for Solving Chemical Kinetics. Computers and Chemical
601 Engineering 26, 1567–1579. doi:[10.1016/S0098-1354\(02\)00128-X](https://doi.org/10.1016/S0098-1354(02)00128-X).

602

603 Eastman, E. D., 1929. Specific heats of gases at high temperatures. Tech. Paper 445, Bureau of
604 Mines.

605

606 Forget, F., Pierrehumbert, R.T., 1997. Warming early Mars with carbon dioxide clouds that
607 scatter infrared radiation. Science 278, 1273–1276. doi:[10.1126/science.278.5341.1273](https://doi.org/10.1126/science.278.5341.1273)

608

609 Forster, P. M. de F., K. P. Shine, 1997. Radiative forcing and temperature trends from
610 stratospheric ozone changes. JGR 102(D9), 10841–10855. doi:[10.1029/96JD03510](https://doi.org/10.1029/96JD03510)

611

612 Forster, P. M., et al., 2011. Evaluation of radiation scheme performance within chemistry climate
613 models. JGR 116, D10302. doi:[10.1029/2010JD015361](https://doi.org/10.1029/2010JD015361)

614

615 Fox, J.L., 2003. Effect of H₂ on the Martian ionosphere: Implications for atmospheric evolution.
616 JGR 108(A6), 1223. doi:[10.1029/2001JA000203](https://doi.org/10.1029/2001JA000203)

617

618 François, L.M., Gérard, J.C., 1988. Ozone, climate and biospheric environment in the ancient
619 oxygen-poor atmosphere. Planet. Space Sci. 36, 1391–1414. doi:[0.1016/0032-](https://doi.org/10.1016/0032-0633(88)90007-4)
620 [0633\(88\)90007-4](https://doi.org/10.1016/0032-0633(88)90007-4)

621

622 Grott, M., Morschhauser, A., Breuer, D., Hauber, E., 2011. Volcanic outgassing of CO₂ and H₂O
623 on Mars. *Earth Planet. Sci. Lett.* 308, 391–400. doi:[10.1016/j.epsl.2011.06.014](https://doi.org/10.1016/j.epsl.2011.06.014)
624

625 Gruszka, M., Borysow, A., 1998. Computer simulation of the far infrared collision induced
626 absorption spectra of gaseous CO₂. *Mol. Phys.* 93, 1007–1016.
627 doi:[10.1080/002689798168709](https://doi.org/10.1080/002689798168709)
628

629 Halvey, I., Zuber, M.T., Schrag, D.P., 2007. A Sulfur Dioxide Climate Feedback on Early Mars.
630 *Science* 318, 1903–1907. doi:[10.1126/science.1147039](https://doi.org/10.1126/science.1147039)
631

632 Halevy, I., Pierrehumbert, R. T., and Schrag, D. P., 2009. Radiative transfer in CO₂-rich
633 paleoatmospheres. *JGR* 114, D18112. doi:[10.1029/2009JD011915](https://doi.org/10.1029/2009JD011915)
634

635 Hauglustaine, D.A., Granier, C., Brasseur, G.P., Mégie, G., 1994. The importance of atmospheric
636 chemistry in the calculation of radiative forcing on the climate system. *JGR* 99(D1), 1173–
637 1186. doi:[10.1029/93JD02987](https://doi.org/10.1029/93JD02987)
638

639 Hiscox, J.A., B.L. Lindner, 1997. Ozone and planetary habitability. *Journal of the British*
640 *Interplanetary Society* 50, 109–114.
641

642 Hunten, D., 1993. Atmospheric Evolution of the Terrestrial Planets. *Science* 259, 915–920.
643 doi:[10.1126/science.259.5097.915](https://doi.org/10.1126/science.259.5097.915)

644

645 Inn, E.C.Y., 1974. Rate of recombination of oxygen atoms and CO at temperatures below
646 ambient. *J. Chem. Phys.* 61, 1589–1590. doi:[10.1063/1.1682139](https://doi.org/10.1063/1.1682139)

647

648 Johnson, R.E., Combi, M.R., Fox, J.L., Ip, W.H., Leblanc, F., McGrath, M.A., Shematovich, V.I.,
649 Strobel, D.F., Waite, J.H., 2008. Exospheres and Atmospheric Escape. *Space Science*
650 *Reviews* 139, 355–397. doi:[10.1007/s11214-008-9415-3](https://doi.org/10.1007/s11214-008-9415-3)

651

652 Johnson, S.S., Mischna, M.A., Grove, T.L., Zuber, M.T., 2008. Sulfur-induced greenhouse
653 warming on Early Mars. *JGR* 113, E08005. doi:[10.1029/2007JE002962](https://doi.org/10.1029/2007JE002962)

654

655 Johnson, S.S., Pavlov, A.A., Mischna, M.A., 2009. Fate of SO₂ in the ancient Martian
656 atmosphere: Implications for transient greenhouse warming. *JGR* 114, E11011.
657 doi:[10.1029/2008JE003313](https://doi.org/10.1029/2008JE003313)

658

659 Kasting, J.F., Liu, S.C., Donahue, T.M., 1979. Oxygen Levels in the Prebiological Atmosphere.
660 *JGR* 84(C6), 3097–3107. doi:[10.1029/JC084iC06p03097](https://doi.org/10.1029/JC084iC06p03097)

661

662 Kasting, J.F., Donahue, T.M., 1980. The Evolution of Atmospheric Ozone. *JGR* 85(C6), 3255–
663 3263. doi:[10.1029/JC085iC06p03255](https://doi.org/10.1029/JC085iC06p03255)

664

665 Kasting, J. F., Walker, J.C.G., 1981. Limits on Oxygen Concentration in the Prebiological

666 Atmosphere and the Rate of Abiotic Fixation of Nitrogen. JGR 86(C2), 1147–1158.
667 doi:[10.1029/JC086iC02p01147](https://doi.org/10.1029/JC086iC02p01147)
668

669 Kasting, J. F., Holland, H.D., Pinto, J.P., 1985. Oxidant Abundances in Rainwater and the
670 Evolution of Atmospheric Oxygen. JGR 90(D6), 10497–10510.
671 doi:[10.1029/JD090iD06p10497](https://doi.org/10.1029/JD090iD06p10497)
672

673 Kasting, J. F., 1991. CO₂ Condensation and the Climate of Early Mars. Icarus 94, 1–13.
674 doi:[10.1016/0019-1035\(91\)90137-I](https://doi.org/10.1016/0019-1035(91)90137-I)
675

676 Kasting, J.F., 1995. O₂ concentrations in dense primitive atmospheres: commentary. Planet.
677 Space Sci. 43, 11–13. doi:[10.1016/0032-0633\(94\)00203-4](https://doi.org/10.1016/0032-0633(94)00203-4)
678

679 Kasting, J.F., 1997. Warming Early Earth and Mars. Science 276, 1213–1215.
680 doi:[10.1126/science.276.5316.1213](https://doi.org/10.1126/science.276.5316.1213)
681

682 Kelly, N. J., et al., 2006. Seasonal polar carbon dioxide frost on Mars: CO₂ mass and columnar
683 thickness distribution. JGR 111, E03S07. doi:[10.1029/2006JE002678](https://doi.org/10.1029/2006JE002678)
684

685 Kiehl, J.T., Trenberth, K.E., 1997. Earth's Annual Global Mean Energy Budget. Bull. Amer.
686 Meteor. Soc., 78, 197-208. doi:[10.1175/1520-0477\(1997\)078%3C0197:EAGMEB
687 %3E2.0.CO;2](https://doi.org/10.1175/1520-0477(1997)078%3C0197:EAGMEB%3E2.0.CO;2)

688

689 Krasnopolsky, V.A., 2006. Photochemistry of the martian atmosphere: Seasonal, latitudinal, and
690 diurnal variations. *Icarus* 185, 153–170. doi:[10.1016/j.icarus.2006.06.003](https://doi.org/10.1016/j.icarus.2006.06.003)

691

692 Kuntz, M., Höpfner, M., 1999. Efficient line-by-line calculation of absorption coefficients.
693 *JQSRT* 63, 97–114. doi:[10.1016/S0022-4073\(98\)00140-X](https://doi.org/10.1016/S0022-4073(98)00140-X)

694

695 Kurucz R.L., 1992. Synthetic infrared spectra in infrared solar physics. In: Rabin D.M., Jefferies
696 J.T., (Eds.), *IAU Symposium*, 154. Kluwer Academic Press, Norwell, MA.

697

698 Lebonnois, S., Hourdin, F., Eymet, V., Crespin, A., Fournier, R., Forget, F., 2010. Superrotation
699 of Venus' atmosphere analyzed with a full general circulation model. *JGR* 115, E06006.
700 doi:[10.1029/2009JE003458](https://doi.org/10.1029/2009JE003458).

701

702 Lemmon, E.W., Huber, M.L., McLinden, M.O., 2010. NIST Standard Reference Database 23:
703 Reference Fluid Thermodynamic and Transport Properties-REFPROP, Version 9.0, National
704 Institute of Standards and Technology, Standard Reference Data Program, Gaithersburg.

705

706 Letchworth, K., Benner, D., 2007. Rapid and accurate calculation of the Voigt function. *JQSRT*
707 107, 173–192. doi:[10.1016/j.jqsrt.2007.01.052](https://doi.org/10.1016/j.jqsrt.2007.01.052)

708

709 Levy, H., 1971. Normal Atmosphere: Large Radical and Formaldehyde Concentrations
710 Predicted. *Science* 173, 141–143. doi:[10.1126/science.173.3992.141](https://doi.org/10.1126/science.173.3992.141)
711

712 Li, H., Ji, X., Yan, J., 2006. A new modification on RK EOS for gaseous CO₂ and gaseous
713 mixtures of CO₂ and H₂O. *Int. J. Energy Res.* 30, 135–148. doi:[10.1002/er.1129](https://doi.org/10.1002/er.1129)
714

715 Liou, KN., 2002. An introduction to atmospheric radiation. 2nd ed., Academic Press. p. 126
716

717 López-Valverde, M., Edwards, D., López-Puertas, M., Roldán, C., 1998. Non-local
718 thermodynamic equilibrium in general circulation models of the Martian atmosphere 1.
719 Effects of the local thermodynamic equilibrium approximation on thermal cooling and solar
720 heating. *JGR* 103, 16799–16811. doi:[10.1029/98JE01601](https://doi.org/10.1029/98JE01601)
721

722 Manga, M., Patel, A., Dufek, J., Kite, E.S., 2012. Wet surface and dense atmosphere on early
723 Mars suggested by the bomb sag at Home Plate Mars. *Geophys. Res. Lett.* 39, L01202.
724 doi:[10.1029/2011GL050192](https://doi.org/10.1029/2011GL050192)
725

726 McElroy, M.B., Donahue, T.M., 1972. Stability of the Martian atmosphere. *Science* 177, 986–
727 988. doi:[10.1126/science.177.4053.986](https://doi.org/10.1126/science.177.4053.986)
728

729 Meadows, V. S., Crisp, D., 1996. Ground-based near-infrared observations of the Venus
730 nightside: The thermal structure and water abundance near the surface. JGR 101(E2), 4595–
731 4622. doi:[10.1029/95JE03567](https://doi.org/10.1029/95JE03567)
732

733 Minschwaner, K., Anderson, G.P., Hall, L.A., Yoshino, K. 1992. Polynomial coefficients for
734 calculating O₂ Schumann-Runge cross sections at 0.5 cm⁻¹ resolution. JGR 97(D9), 10103–
735 10108. doi: [10.1029/92JD00661](https://doi.org/10.1029/92JD00661)
736

737 Mischna, M.A., Kasting, J.F., Pavlov, A., Freedman, R., 2000. Influence of carbon dioxide
738 clouds on early martian climate. Icarus 145, 546–554. doi:[10.1006/icar.2000.6380](https://doi.org/10.1006/icar.2000.6380)
739

740 Montmessin, F., et al., 2006. Subvisible CO₂ ice clouds detected in the mesosphere of Mars.
741 Icarus 183, 403–410. doi:[10.1016/j.icarus.2006.03.015](https://doi.org/10.1016/j.icarus.2006.03.015)
742

743 Montmessin, F., et al., 2011. A layer of ozone detected in the nightside upper atmosphere of
744 Venus. Icarus 216, 82–85. doi:[10.1016/j.icarus.2011.08.010](https://doi.org/10.1016/j.icarus.2011.08.010)
745

746 Nair, H., Allen, M., Anbar, A.D., Yung, Y.L., Clancy, R.T., 1994. A Photochemical Model of the
747 Martian Atmosphere. Icarus 111, 124–150. doi:[10.1006/icar.1994.1137](https://doi.org/10.1006/icar.1994.1137)
748

749 Neukum , G., et al., 2010. The geologic evolution of Mars: Episodicity of resurfacing events and
750 ages from cratering analysis of image data and correlation with radiometric ages of Martian

751 meteorites. Earth Planet. Sci. Lett. 294, 204–222. doi:[10.1016/j.epsl.2009.09.006](https://doi.org/10.1016/j.epsl.2009.09.006)
752
753 Old, J.G., Gentili, K.L., Peck, E.R., 1971. Dispersion of Carbon Dioxide. J. Opt. Soc. Am. 61,
754 89–90. doi:[10.1364/JOSA.61.000089](https://doi.org/10.1364/JOSA.61.000089)
755
756 Parkinson, T.D., Hunten, D.M., 1972. Spectroscopy and Aeronomy of O₂ on Mars. J. Atm. Sci.
757 29, 1380–1390. doi:[10.1175/1520-0469\(1972\)029%3C1380:SAAOOO%3E2.0.CO;2](https://doi.org/10.1175/1520-0469(1972)029%3C1380:SAAOOO%3E2.0.CO;2)
758
759 Perrin, M.Y., Hartmann, J.M., 1989. Temperature-dependent measurements and modeling of
760 absorption by CO₂–N₂ mixtures in the far line-wings of the 4.3-μm CO₂ band. JQSRT 42,
761 311–317. doi:[10.1016/0022-4073\(89\)90077-0](https://doi.org/10.1016/0022-4073(89)90077-0)
762
763 Pollack, J.B., Kasting, J.F., Rochardson, S.M., Poliakoff, K., 1987. The case for a wet, warm
764 climate on early Mars. Icarus 71, 203–224. doi:[10.1016/0019-1035\(87\)90147-3](https://doi.org/10.1016/0019-1035(87)90147-3)
765
766 Quine, B.M., and Drummond, J.R., 2002. GENSPECT: a line-by-line code with selectable
767 interpolation error tolerance. JQSRT 74, 147–165. doi:[10.1016/S0022-4073\(01\)00193-5](https://doi.org/10.1016/S0022-4073(01)00193-5)
768
769 Ribas, I., et al., 2010. Evolution of the Solar Activity Over Time and Effects on Planetary
770 Atmospheres. II. κ¹ Ceti, an Analog of the Sun when Life Arose on Earth. Astrophys. J. 714,
771 384–395. doi:[10.1088/0004-637X/714/1/384](https://doi.org/10.1088/0004-637X/714/1/384)
772

773 Richardson, M.I., Mischna, M.A., 2005. Long-term evolution of transient liquid water on Mars.
774 JGR 110, E03003. doi:[10.1029/2004JE002367](https://doi.org/10.1029/2004JE002367)
775

776 Robbins, S.J., Achille, G.D., Hynek, B.M., 2011. The volcanic history of Mars: High-resolution
777 crater-based studies of the calderas of 20 volcanoes. Icarus 211, 1179–1203.
778 doi:[10.1016/j.icarus.2010.11.012](https://doi.org/10.1016/j.icarus.2010.11.012)
779

780 Rothman, L.S., et al., 2009. The HITRAN 2008 molecular spectroscopic database. JQSRT 110,
781 533–572. doi:[10.1016/j.jqsrt.2009.02.013](https://doi.org/10.1016/j.jqsrt.2009.02.013)
782

783 Rosenqvist, J., Chassefière, E., 1995. Inorganic chemistry of O₂ in a dense primitive atmosphere.
784 Planet. Space Sci. 43, 3–10. doi:[10.1016/0032-0633\(94\)00202-3](https://doi.org/10.1016/0032-0633(94)00202-3)
785

786 Sander S.P., et al., 2011. Chemical Kinetics and Photochemical Data for Use in Atmospheric
787 Studies, Evaluation Number 17, JPL Publication 10-6, Jet Propulsion Laboratory, Pasadena,
788 CA.
789

790 Sandu, A., Daescu, D., Carmichael, G.R., 2003. Direct and Adjoint Sensitivity Analysis of
791 Chemical Kinetic Systems with KPP: I – Theory and Software Tools, Atmospheric
792 Environment 37, 5083–5096. doi:[10.1016/j.atmosenv.2003.08.019](https://doi.org/10.1016/j.atmosenv.2003.08.019)
793

794 Segura, A., Meadows, V. S., Kasting, J. F., Crisp, D., Cohen, M., 2007. Abiotic formation of O₂

795 and O₃ in high-CO₂ terrestrial atmospheres. A&A 472, 665–679. doi:[10.1051/0004-](https://doi.org/10.1051/0004-6361:20066663)
796 [6361:20066663](https://doi.org/10.1051/0004-6361:20066663)
797
798 Selsis, F., Despois, D., Parisot, J.-P., 2002. Signature of life on exoplanets: Can Darwin produce
799 false positive detections? A&A 388, 985–1003. doi:[10.1051/0004-6361:20020527](https://doi.org/10.1051/0004-6361:20020527)
800
801 Span, R., Wagner, W., J., 1996. A New Equation of State for Carbon Dioxide Covering the Fluid
802 Region from the Triple-Point Temperature to 1100 K at Pressures up to 800 MPa. Phys.
803 Chem. Ref. Data 25, 1509–11596. doi:[10.1063/1.555991](https://doi.org/10.1063/1.555991)
804
805 Squyres, S.W., Kasting, J.F., 1994. Early Mars: How Warm and How Wet? Science 265, 744–
806 749. doi:[10.1126/science.265.5173.744](https://doi.org/10.1126/science.265.5173.744)
807
808 Tian, F., Claire, M.W., Haqq-Misra, J.D., Smith, M., Crisp, D.C., Catling, D., Zahnle, K.,
809 Kasting, J.F., 2010. Photochemical and climate consequences of sulfur outgassing on early
810 Mars. Earth Planet. Sci. Lett. 295, 412–418. doi:[10.1016/j.epsl.2010.04.016](https://doi.org/10.1016/j.epsl.2010.04.016)
811
812 Tonkov, M.V., et al., 1996. Measurements and empirical modeling of pure CO₂ absorption in the
813 2.3- μ m region at room temperature: Far wings, allowed and collision-induced bands. Appl.
814 Opt. 35, 4863–4870. doi:[10.1364/AO.35.004863](https://doi.org/10.1364/AO.35.004863)
815
816 Toon, O.B., McKay, C.P., Ackerman, T.P., Santhanam, K., 1989. Rapid calculation of radiative

817 heating rates and photodissociation rates in inhomogeneous multiple scattering atmospheres.
818 JGR 94(D13), 16287–16301. doi:[10.1029/JD094iD13p16287](https://doi.org/10.1029/JD094iD13p16287)
819

820 Tvorogov, S.D, Rodimova, O.B., Nesmelova, L.I., 2005. On the correlated *k*-distribution
821 approximation in atmospheric calculations. Opt. Eng. 44, 071202. doi:[10.1117/1.1955318](https://doi.org/10.1117/1.1955318)
822

823 Wells, R.J., 1999. Rapid approximation to the Voigt/Faddeeva function and its derivatives.
824 JQSRT 64, 29–48. doi:[10.1016/S0022-4073\(97\)00231-8](https://doi.org/10.1016/S0022-4073(97)00231-8)
825

826 Wordsworth, R., Forget, F., Eymet, V., 2010a. Infra-red collision-induced and far-line absorption
827 in dense CO₂ atmospheres. Icarus 210, 992–997. doi:[10.1016/j.icarus.2010.06.010](https://doi.org/10.1016/j.icarus.2010.06.010)
828

829 Wordsworth, R., Forget, F., Selsis, F., Madeleine, J.-B., Millour, E., Eymet, V., 2010b. Is Gliese
830 581d habitable? Some constraints from radiative-convective climate modeling. A&A 522,
831 A22. doi:[10.1051/0004-6361/201015053](https://doi.org/10.1051/0004-6361/201015053)
832

833 Yung Y. L., Nair H., Gerstell M. F., 1997. CO₂ Greenhouse in the Early Martian Atmosphere:
834 SO₂ Inhibits Condensation. Icarus 130, 222–224. doi:[10.1006/icar.1997.5808](https://doi.org/10.1006/icar.1997.5808)
835

836 Zahnle, K. J., Haberle, R. M., Catling, D. C., Kasting, J. F., 2008. Photochemical instability of
837 the ancient Martian atmosphere. JGR 113, E11004. doi:[10.1029/2008JE003160](https://doi.org/10.1029/2008JE003160)

Figure1

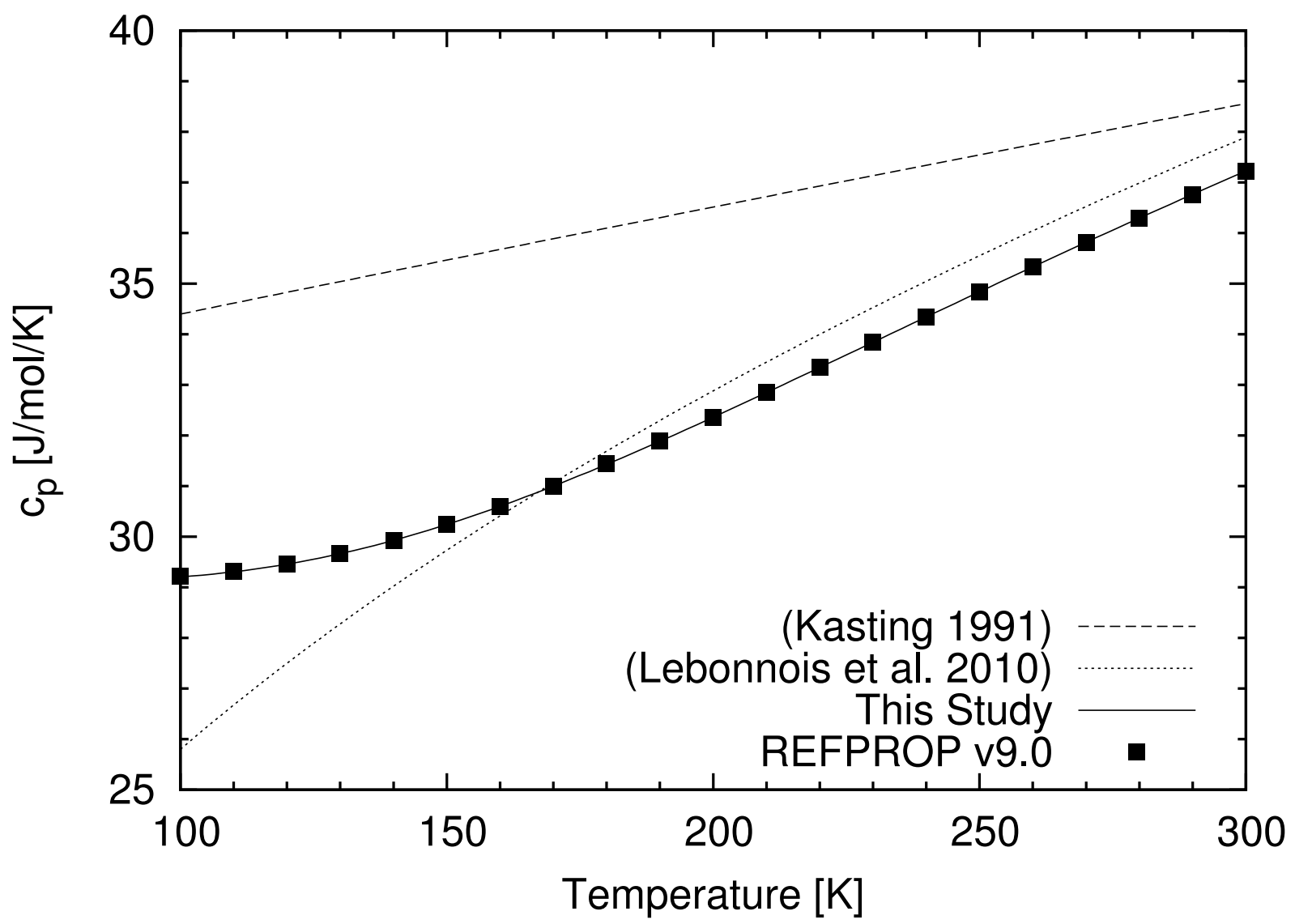


Figure2a

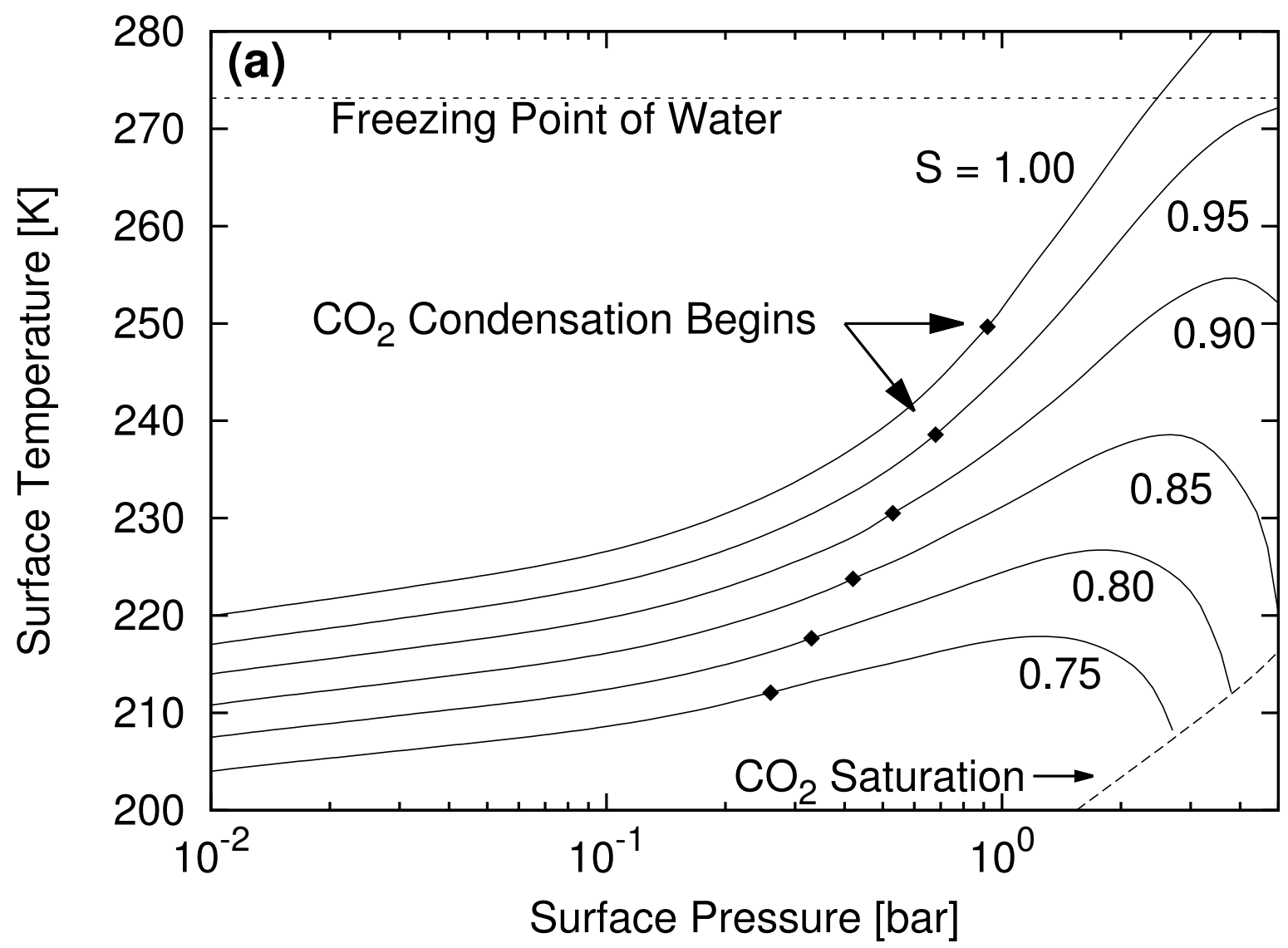


Figure2b

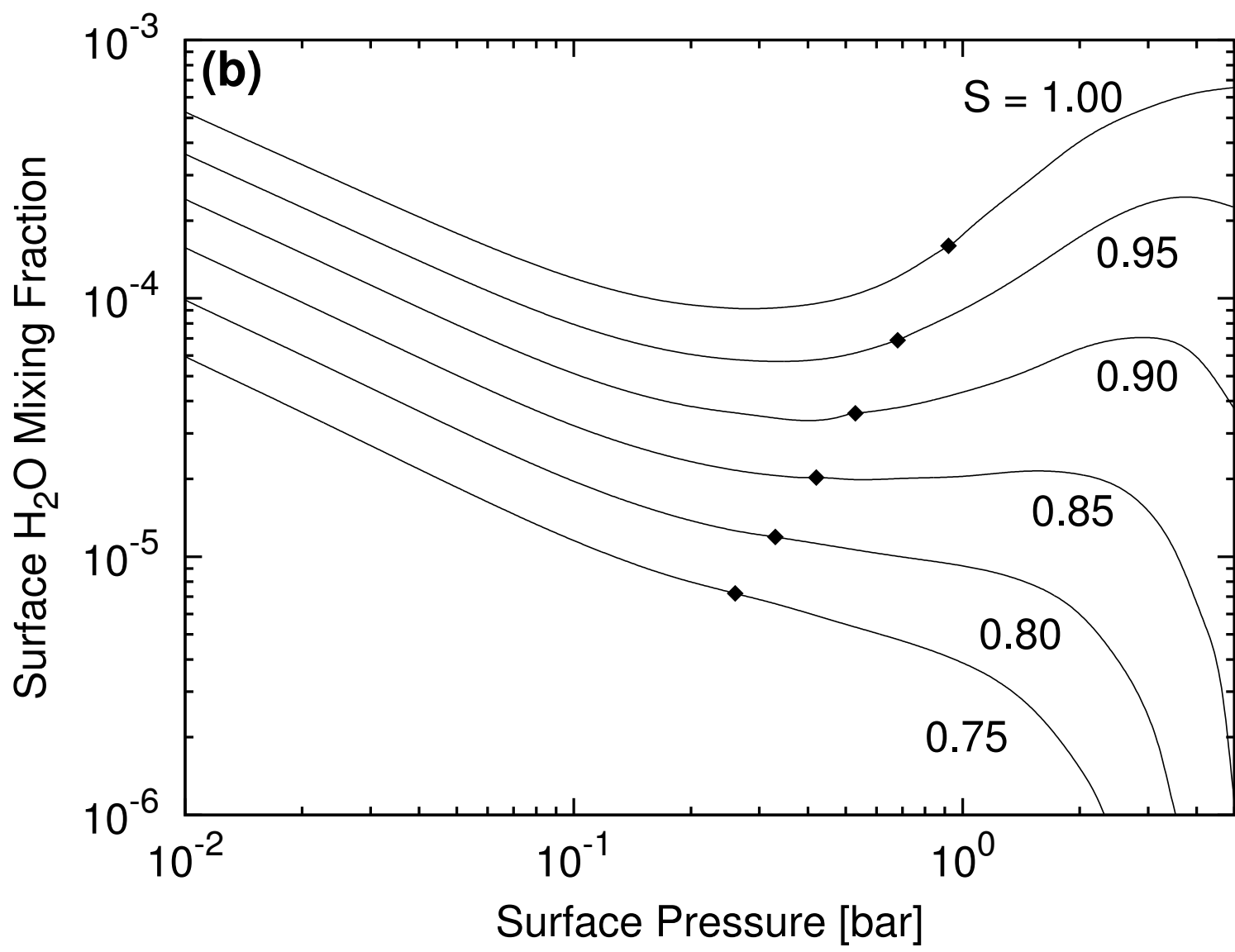


Figure3

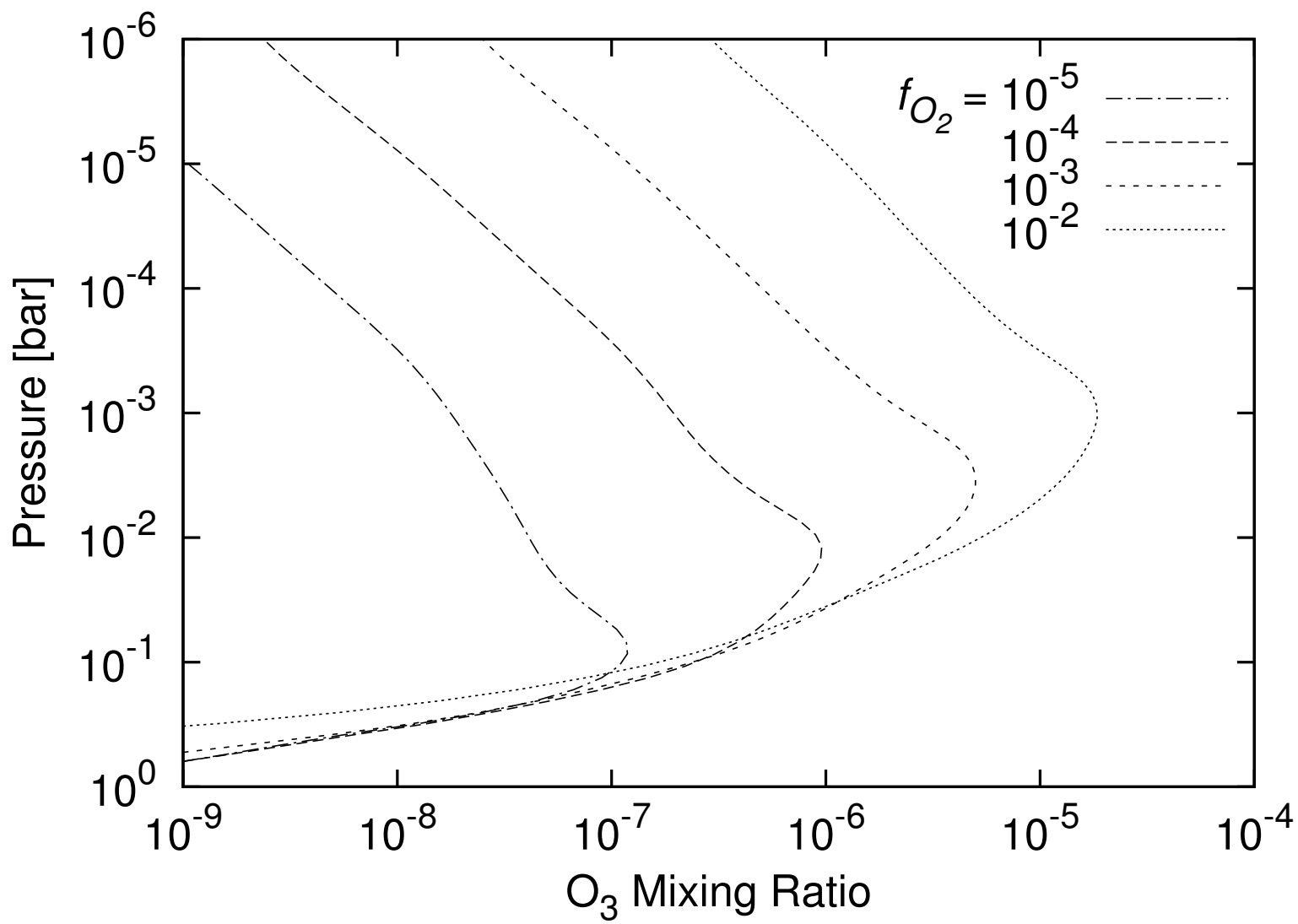


Figure4

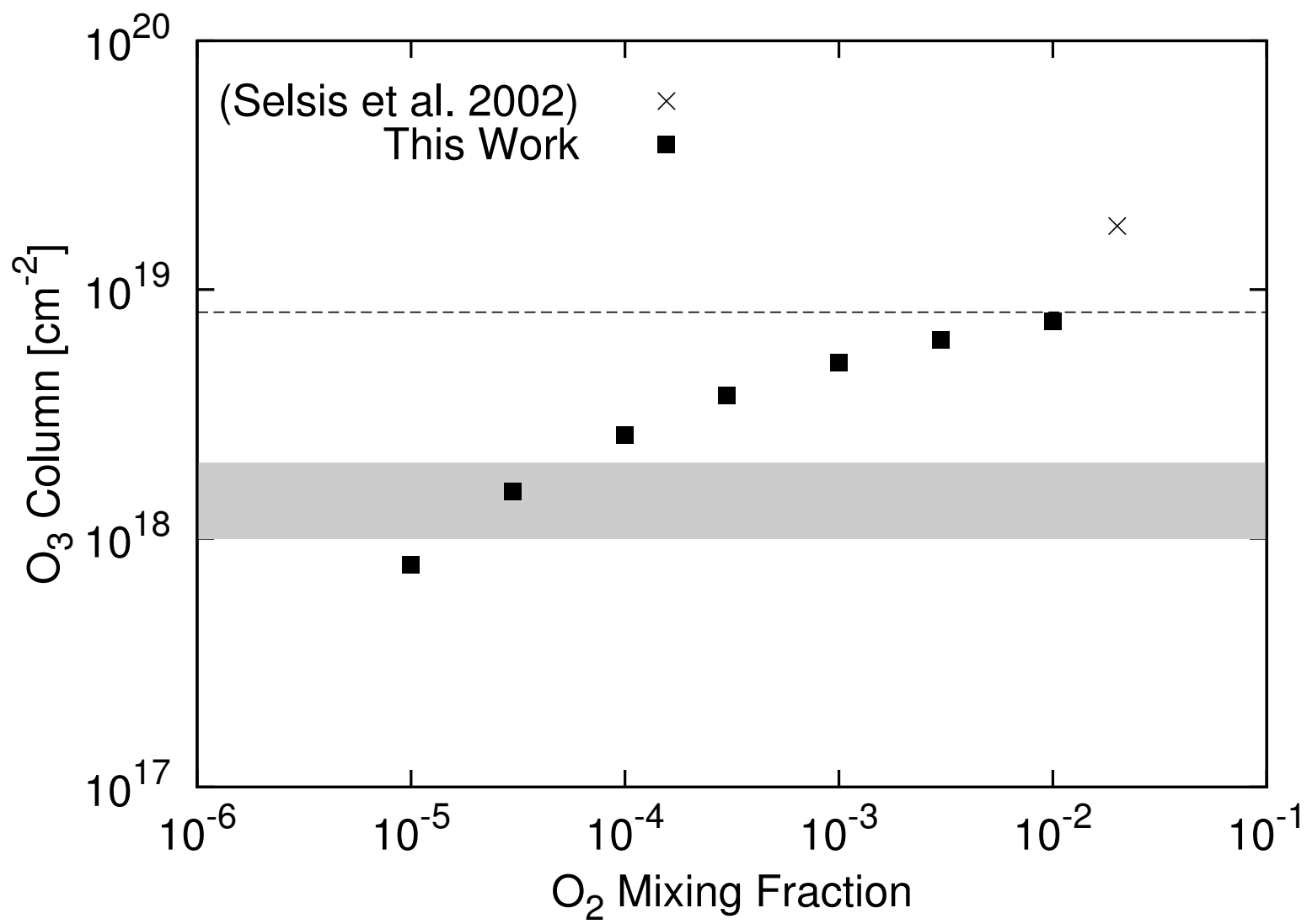


Figure5

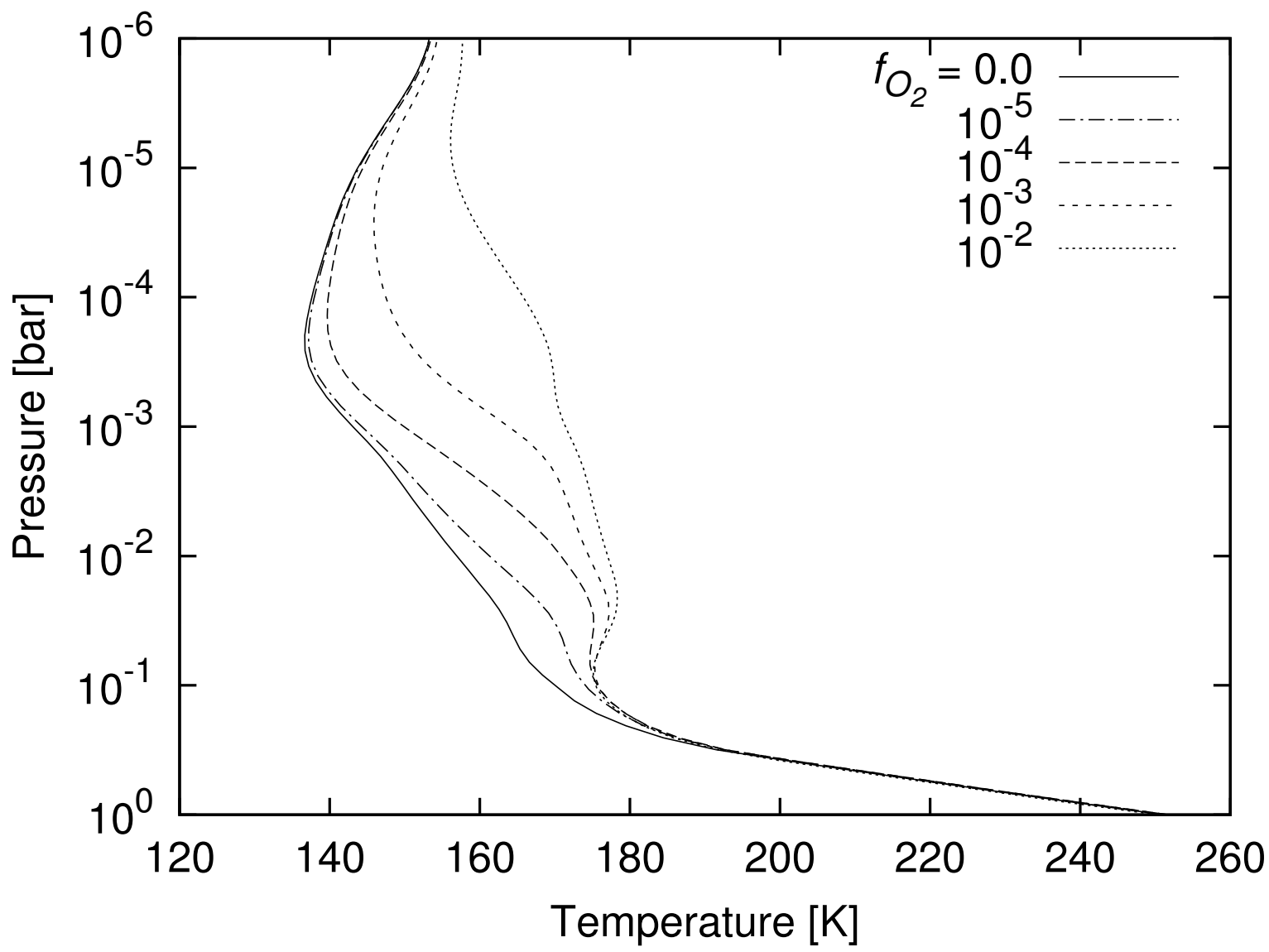


Figure6

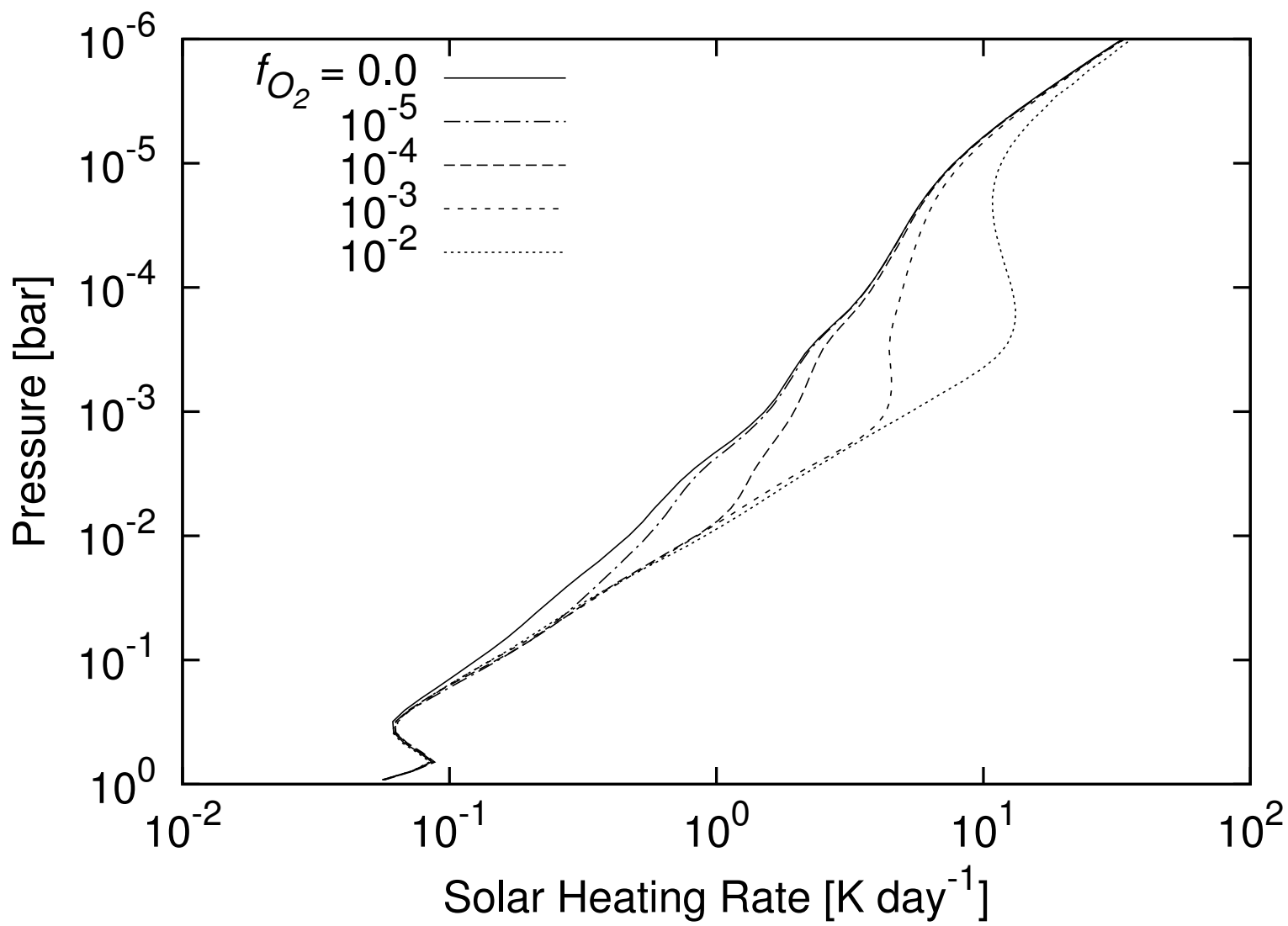
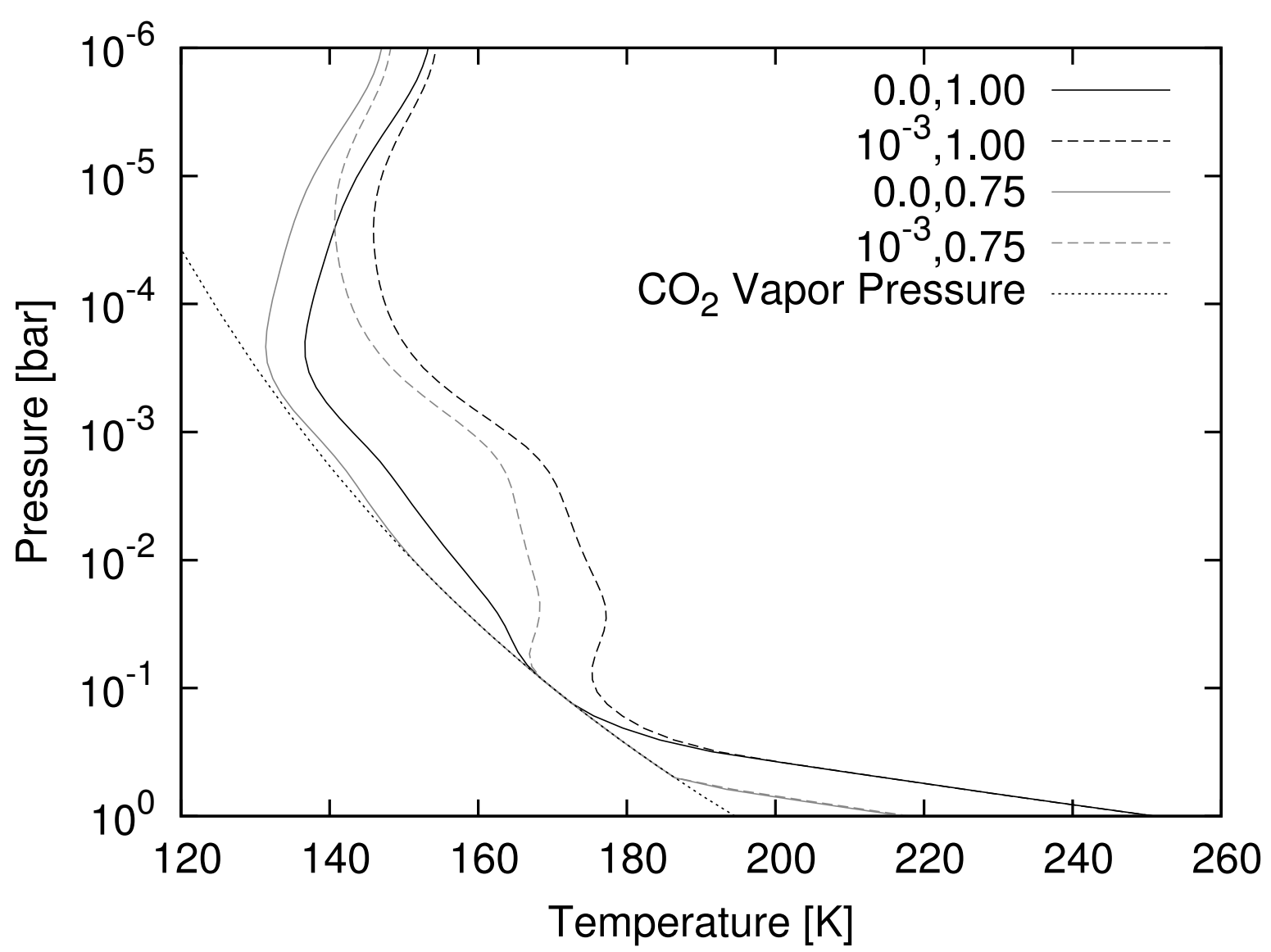
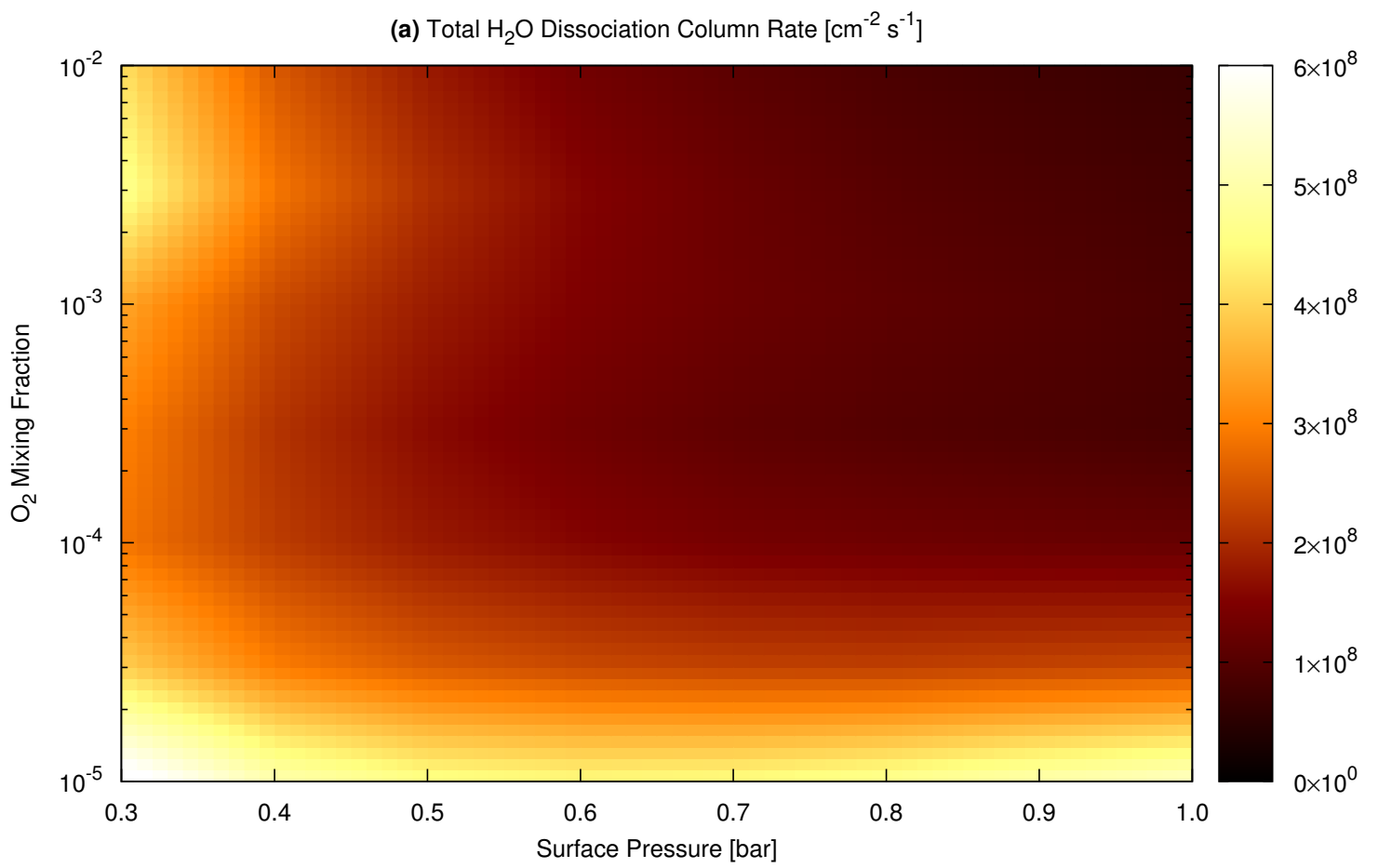
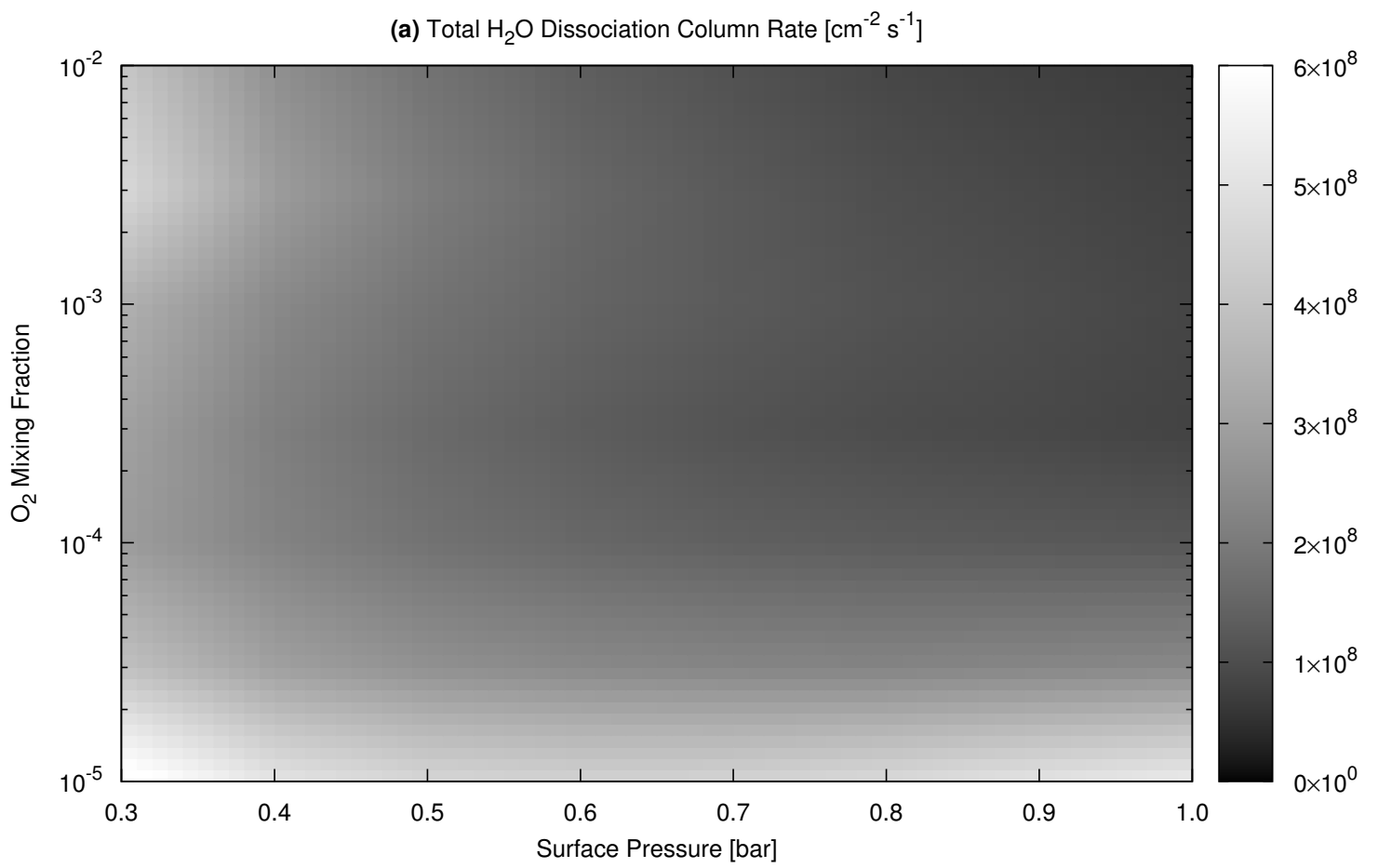
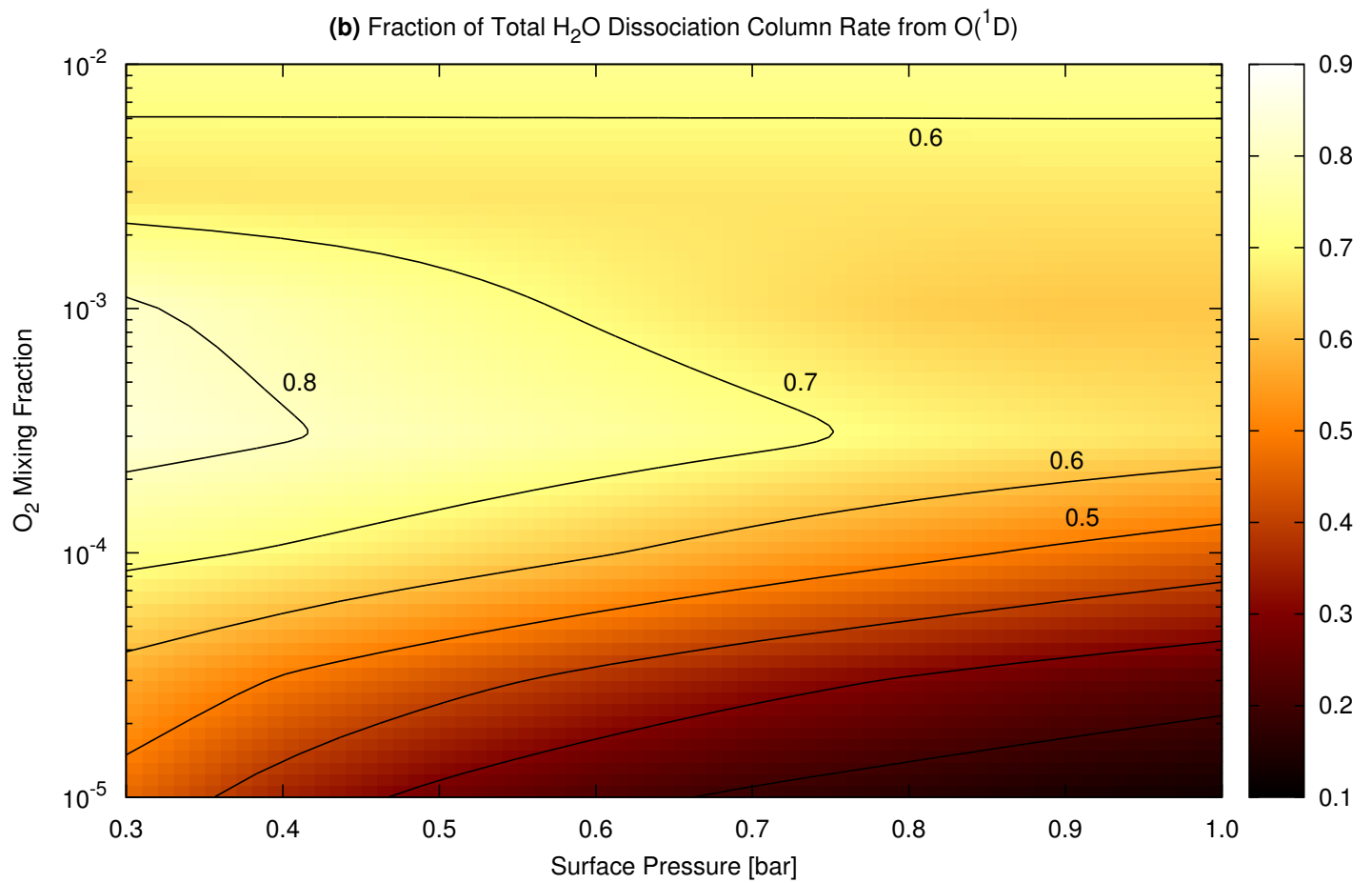


Figure7









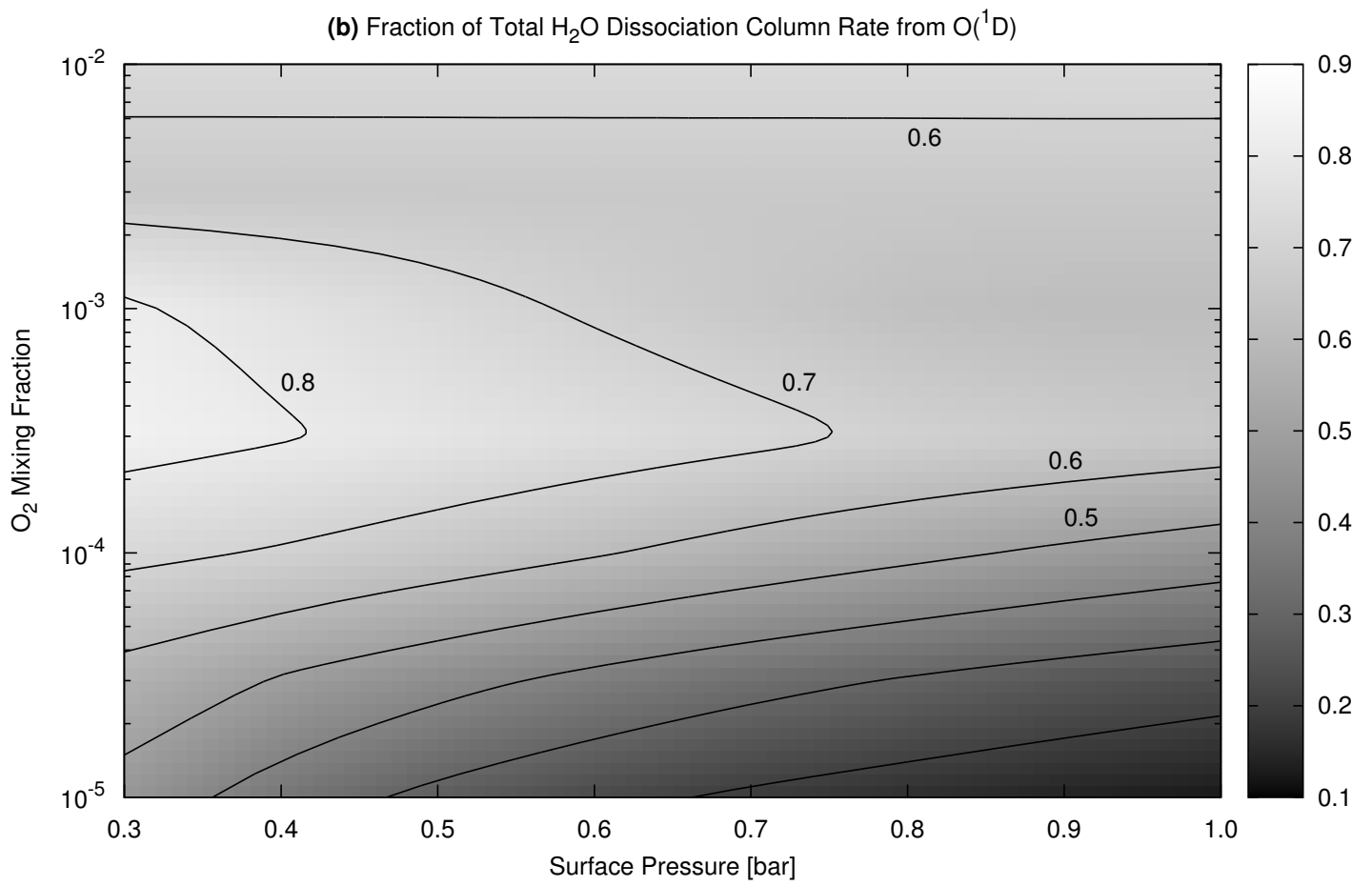


Figure9

